IN THE NAME OF GOD

THE COMPASSIONATE, THE MERCIFUL

DOCTORAL DISSERTATION

Application of Acoustic Tomography System for Monitoring Streamflow and Suspended Sediment Concentration in a Mountainous River and Tidal Estuary

(山地河川と感潮河口域における河川流量と浮遊土砂濃度の

モニタリングに対する音響トモグラフィーの適用)

March 2017

Department of Civil and Environmental Engineering

Graduate School of Engineering

Hiroshima University

MASOUD BAHREINIMOTLAGH

Acknowledgements

First and above all, I praise **God**, the almighty for providing me this opportunity and granting me the capability to proceed successfully. This thesis appears in its current form due to the assistance and guidance of several people. I would therefore like to offer my sincere thanks to all of them.

I would like to express my sincere gratitude to my advisor Prof. **Kiyosi Kawanisi** for the continuous support during my Ph.D study and related research, for his patience, motivation and immense knowledge. His guidance helped me throughout the research and writing of this thesis. I could not imagine having a better advisor and mentor for my Ph.D study.

In addition to my advisor, I would like to thank the rest of my thesis committee: Prof. **Yoshihisa Kawahara** and Prof. **Yasuaki Doi**, for their insightful comments and encouragement and also for the hard questioning, which encouraged me to widen my research from various perspectives.

I gratefully thank Prof. **Arata Kaneko** for his invaluable insights into the application of acoustic tomography in coastal regions. Prof. Kaneko shared two decades of his experiences with me and opened a new window to my future studies.

Special thanks are extended to Prof. **Noriaki Gohda** for his kind advice and suggestions on acoustic tomography system design and construction. Prof. Gohda has supported me not only academically but also emotionally along the rough road to finishing this thesis.

It is a pleasure to thank those who made this thesis possible. In particular, I gratefully thank my friends Dr. **Mohammad Soltaniasl** and **Junya Kagami** who helped me during my doctoral study.

I warmly thank and appreciate **my parents and my brother** for supporting me spiritually throughout writing this thesis and in my life in general.

Finally, I would like to thank my lovely wife. Dear **Elaheh**, without your support and encouragement I could not have finished this work. It was you who maintained the fundamentals of our family and I understand that it was difficult for you; therefore, can I just say thank you for everything and may God give you all the best in return.

MASOUD BAHREINIMOTLAGH

HIROSHIMA UNIVERSITY

March 2017

Table of Contents

List of Figures

List of Tables

List of Notations

Symbols	
Q	Flow rate
c_1, c_2	Constants coefficient of Rating Curve method
H	Water level
v	Mean velocity
u	Mean velocity through the sound ray path
θ	Angle between the ray path and the stream line
L	Horizontal distance between the transducers
h_m	Mean water elevation
A_B	Function of cross section bathymetry
Z_b	Elevation of the riverbed along the transmission line
δQ	Error of streamflow
δQ_{h_m}	Error of water depth
δQ_{A_B}	Error of river bathymetry
δQ_{u_m}	Error of section-average-velocity
δQ_θ	Error the angle between the transmission line and the stream axis
α_s	Attenuation by sediments
R	Distance
ξ_s	Scattering loss
ξ_v	Viscous absorption
SSC	Suspended sediment concentration
r	Distance
ϵ	Volume concentration of particulate
k	Acoustic wave number
β	Reciprocal of the viscous skin depth

ω	Angular frequency of the incident pressure wave
a	Particle radius
ρ_s	Density of the particulate
ρ_0	Density of the water
α_w	Attenuation due to water
E	Echo level (in counts)
K_c, C	Signal calibration coefficients
ψ	Near-field coefficient
SNR	Signal-to-noise ratio
t	Time
$t_i^{\pm}$	Travel time of sound between two acoustic stations
C_0	Reference sound speed
δC	Deviation from the reference
n	Unit vector tangent to the ray path
C_m	Mean sound speed
t_{Down}	Arrival time at downstream station
t_{Up}	Arrival time at upstream station
G_p	Processing gain
T_p	Period of M sequence
T_r	Width of one digit of M sequence
T_a	Time resolution of the FATS
f	Frequency
$\emptyset$	Angle between two cross paths
$\delta\theta_\emptyset$	The error of the angle between two transmission lines
φ	Angle of the ray measured from the horizontal axis *r*
ϵ_{xx}, ϵ_{xy}, ϵ_{yx}, and ϵ_{yy}	Eddy viscosity coefficients

Abstract

The amount of water passing through a cross section of river, known as the discharge, is seldom measured directly. In most cases one measures and records the water level (stage). Stage records are subsequently transformed to discharge by means of an estimated stage-discharge relationship, referred to as the Rating Curve (RC) method. However, there are some factors that contribute to the imprecision in discharge data (e.g. inaccurate stage measurement, low time-resolution in the stage recording, and so on). Moreover, when the river reach is hydraulically influenced by backwater effects, such as dams, lakes or the sea, it is impossible to establish. Recently, several innovative velocity-monitoring systems were utilized to monitor the streamflow. Acoustic Doppler Current Profilers (ADCPs) are the most common instruments for this purpose and are divided into two groups: moving-boat ADCPs and fixed ADCPs. The obvious disadvantage of a moving-boat ADCP is that it cannot measure the streamflow continuously. Fixed H-ADCPs not only have limitations in wide and shallow rivers but also require complex post processing methods, to compute the river discharge. The present study demonstrates the application of the Fluvial Acoustic Tomography System (FATS), which overcomes the restrictions of the previous methods.

The first experiment presents one-month record of flow velocity and river discharge performed by FATS in a mountainous shallow river. The effect of suspended sediment concentration on the FATS signals was also investigated and a primary attempt was made to estimate the cross sectional averaged suspended sediment concentration <SSC>. The flow velocity varied between 0.5 m/s to 1.6 m/s. The streamflow ranged from 50 m^3/s to 260 m^3/s, where the minimum and maximum mean water depths were 0.6 m and 1.42 m, respectively. The streamflow was compared to the RC method. The relative difference was less than ±20 % and the root-mean-square of the residual (RMSR) was 9.42 m^3/s. It was observed that the SSC has a direct influence on the Signal to Noise Ratio (SNR) of the FATS. At low concentrations, when the turbidity was less than 2 FTU, the SNR of upstream and downstream stations was 25 dB and 35 dB, respectively; whereas at the high concentration, when the turbidity exceeded 45 FTU, the SNR decreased dramatically to 6 dB and 12 dB, respectively. A new equation is introduced to convert the SNR of FATS to <SSC>. The

results showed that the maximum <SSC> reached 0.1 kg/m^3 in this period and proportionally the Suspended Sediment Flux (SSF) exceeded 20 kg/s^{-1}. The comparison of SSC measurement by FATS and other methods, such as Optical Backscatter Sensor (OBS) and ADCP, showed that the accuracy of SSC measurement by FATS is low, as the SNR intensity does not only depend on the turbidity but also other factors such as water depth, weeds and bottom shape.

In the second experiment reported in this thesis, the efficiency of the high-frequency (53-kHz) FATS was examined. Furthermore, a new solution using FATS systems with cross-path configuration was proposed to estimate the flow direction. The results showed that the 53-kHz FATS have better velocity resolution and it can be operated in shorter ranges than the 30-kHz FATS. An ADCP was used to validate the angle measurement obtained from FATS system. The angle estimated by FATS varied from 12 to 18 degrees, as well, the coefficient of determination (R^2) between the ADCP and proposed method was 0.78. Then, the river discharge was estimated by both FAT systems and compared to the RC method and moving-boat ADCP estimates. The relative difference of the FATS discharge measurements was less than 10%. In this experiment, an interesting phenomenon was observed. Although this experiment was performed in a freshwater river and the acoustic signals were not influenced by salinity, the signals of FATS were divided by two groups. The ray simulation showed that the river bathymetry affected the propagated signals and the second group arrived about 0.4 ms after the first group. The last observation was made in the Ota Estuary, where the tidal currents and river discharge collide. A numerical model was applied to estimate the flow velocity and compare with the velocity measurement obtained by FATS. The numerical model was compared to both the FATS and ADCP estimates. The flow velocity changed between -0.2 m/s and 0.85 m/s from the landward and seaward sites, respectively. It was concluded that FATS is the reliable instrument to be used as a boundary condition input of the numerical models.

1. Background and purpose

1.1 Study overview

The measurement of river discharge is of paramount importance in issues related to water management. In other words, reliable, accurate and continuous measurement of streamflow is essential for water management purposes in rivers and estuaries.

The traditional way to monitor river discharge is to convert water level to discharge using a Rating Curve (RC) method [1] [2]. The RC method may produce a large error in streamflow estimation. The cost of installation and operation of gauging stations greatly limits the number of river gauging stations installed [3]. For example, the cost for the United States Geological Survey (USGS) to install a gauging station in a river is between US$20,000 and US$35,000. Moreover, the annual operational cost is about US$20,000 [4]. Over the last decade, investigations have shown that the number of gauging stations in the United States is decreasing because of a shortage of funding [5] [6]. Additionally, applications of the RC method are impractical or impossible under complex flow conditions, such as variable backwater, tidal flow, rapid changes in flow, and so on.

RC method

To establish the RC equation, the cross section of river is often divided into a number of sub-cross sections, in each of which a number of flow velocities at different flow depths are measured and averaged, resulting in a mean flow velocity for that sub-cross section (Figure 1-1). The river discharge is then computed as the sum of all mean flow velocities multiplied by sub-cross section area [7]. By plotting the measured discharges against the corresponding stages and drawing the relation between the two quantities using a smooth curve, the RC equation can be established.

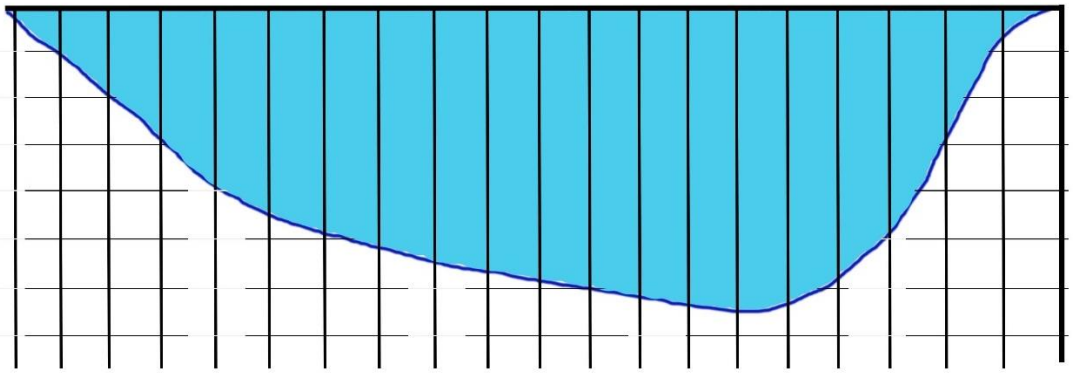

Figure 1-1 River cross section and the sub-cross sections of river.

In this study, well-established RCs can be extracted from stream gauges at the Ozekiyama gauging station. In this study, the RC equations are made by the MLIT (Ministry of Land, Infrastructure, Transport and Tourism, Japan). Eq.(1.1) expresses the *HQ* function that is widely used in Japan:

$$Q = c_1(H - c_2)^2 \tag{1.1}$$

In this equation, c_1 and c_2 are calibration coefficients and H is water level at the gauging station. The power of this equation depends on the cross-sectional shape of the river. In the case of parabolic shapes, the power is quadratic, on the other hand, the rectangular or triangular shapes have different values of power.

usually the Price type-AA current meter is used to measure one component of flow velocity for a small volume of the total flow measuring section. Total flow (river discharge) is determined by multiplying each measured velocity by its contributing flow area. The c_1 and c_2 can be obtained via the regression of the measured discharges against the corresponding water level. Usually, the c_1 and c_2 coefficients depend on the water level. Because the cross sectional shape of a river differs under low and high flow conditions. For example, floodwater not only flows in the main channel but also on the floodplains. Consequently, the measurement should be done for the various water levels. Hence, at least two or three equations are needed for the different ranges of water levels. In this case, depending on the range of the water elevation H m above mean sea level (m a.s.l.), the MLIT proposed the following RC equations for the Ozekiyama gauging station in the 2014 fiscal year:

$$\begin{cases} Q_1(145.97 \le H \le 148.07) = 67.80(H - 145.97)^2 \\ Q_2(148.08 \le H \le 151.94) = 51.31(H - 145.66)^2 \\ Q_3(151.95 \le H \le 154.25) = 39.34(H - 144.76)^2 \end{cases} \tag{1.2}$$

The inter-annual variability of the RCs was usually small. A one-to-one relation is not often observed between the river stage and the discharge in unsteady flow conditions (flood events) because the water surface profile differs in the rising and falling periods. However, the RC uncertainty was trivial at the gauging station because of the large bed slope.

In the 2014 fiscal year, streamflow measurements under low-flow conditions of $H \leq 147.41$ m a.s.l were carried out using the Price-type AA current meter. The current meter was cast from a boat at 10 m intervals across the river. Flow velocity was measured for 20 s at two points in the water column: approximately 20% and 80% of the water depth. For high flows, tracking floats carried out the streamflow measurements. The floats were cast from the Iwai Bridge (Figure 3-1) every 12 m across the river.

Acoustic methods for flow measurement

There are several kinds of acoustic instruments, such as Acoustic Doppler Velocimetry (ADV) [8], Acoustic Doppler Current Profilers (ADCP) [9], Acoustic Doppler Velocity Profilers (ADVP) [14,15] and Acoustic Concentration and Velocity Profilers (ACVP) [12] for performing different experiments. These acoustic instruments have proven to be a reliable way of obtaining high-resolution data, to provide remote and non-intrusive methods of measurements of flow velocities [17,18], discharges [19-21] and profiles of suspended sediment concentration [22-24]. In addition to the traditional stage-discharge RC method the Acoustic Doppler Current Profiler (ADCP) has

evolved to be a useful tool for measuring flow velocity and streamflow since the 1990s [8-11]. The limitations of these current methods of flow rate measurement are presented in Table 1.

Table 1-1 The limitations in flow rate measurement methods.

Method	Limitations
Rating Curve (RC)	-Variation in RC relation due to changes in bathymetry and roughness -Application of this method in the tidal rivers is complex
Moving-boat ADCPs	-Unable to measure the flow rate continuously -Difficulties involving use during high-flow conditions
H-ADCP	-Attenuated acoustic signal in flood events and turbid waters - Several hydraulic parameters are needed

In the present study three types of ADCPs were employed. The general characteristics of these instruments will be reviewed briefly in the next sections.

StreamPro ADCP

Teledyne RD Instruments has developed different types of ADCPs for stream flow measurement in rivers, estuaries and oceans. StreamPro ADCP is operated at 2457.6 kHz and offers a preferred solution for making discharge measurements in small and medium streams with depths up to 2 m (6 m with upgrade) [29,30]. It was previously used in many shallow rivers and estuaries to measure flow velocity and river discharge [31-34]. The StreamPro ADCP is an accurate, rapid-sampling current profiling system designed to operate from a moving boat.

Workhorse ADCP

The WorkHorse ADCP is an accurate, rapid-sampling current profiling system. Workhorse ADCP operates in three different frequencies, 1200 kHz, 600 kHz and 300 kHz and can make measurements in deep rivers and coastal areas [25]. The maximum range of these three types is 19 m, 66 m and 154 m, respectively. This model is also able to attach a boat and measure flow velocity and river discharge [36,37].

AquaDopp Profiler

The Aquadopp Profiler is an inexpensive acoustic tool with a wide range of applications [38,39]. The Aquadopp Profilers are offered with the different acoustic frequencies as 400 kHz, 600 kHz, 1 MHz and 2 MHz to be applied for any body of water, including ocean, estuary or river [40-43]. The instrument is usually used in real-time applications but also includes all parts required for self-contained deployment with data stored to an internal data logger.

In Table 1-2, some of the technical specifications of StreamPro, WHADCP and Aquadopp ADCPs are presented.

Table 1-2 Technical features of StreamPro, WHADCP and AquaDopp Profiler.

Parameter		**StreamPro**	**WHADCP**	**AquaDopp Profiler**
Acoustic frequency		2457.6 kHz	1228.8 kHz	2 MHz
Water velocity measurement	Range	± 5 m/s	± 5 m/s	± 10 m/s
	Accuracy	± 1% of water velocity relative to ADCP, ± 2 mm/s	0.25% of measured velocity ± 0.2 mm/s	1% of measured velocity ± 5 mm/s
	Cell number	1–30	1–128	1–128
	Cell size	0.02–0.2 m	0.05–2 m	0.1–2 m
	Minimum blank distance	0.03 m	0.05 m	0.1 m
Software		WinRiverII	WinRiverII	AquaPro
Power	Voltage consumption	10.5 –18 V	10.5–18 V 1.5 W	9–16 V 0.2–1 W

The ADCPs have range limitations, the signal strength of an acoustic pulse decreases logarithmically with distance from the transducer face. As the signal strength and signal-to-noise ratio (SNR) decreases, the spectral width of the returned signal increases. This increase in spectral width with range causes an increased standard deviation of the measured velocity with range; hence, at some ranges the return echo is unusable. This limiting range is largely dependent on the transducer frequency. Conservative estimates of WHADCP maximum range for several transducer frequencies are presented in Table 1-3.

Table 1-3 The frequency and maximum range of different WHADCPs.

WHADCP frequency (kHz)	Range (m)
300	118.8
600	48
1200	15.4

ADCP Uncertainty

The ADCP is an acoustic instrument best known for its capability to measure profiles of water velocity. There are two error types contribute to velocity uncertainty; bias errors, which are called systematic errors and random error. Data averaging can reduce random error but cannot for bias error. A thorough understanding of these two types of errors is a crucial prerequisite to the assessment of ADCP velocity and discharge measurement accuracy [44,45].

A. Random error

• Pulse length—the shorter the pulse length for a given frequency in a narrow-band ADCP, increases the random error.

• Transmit frequency—the lower the frequency at a given pulse length (or lag distance), increases the random error.

• Signal-to-noise ratio—the lower the signal-to-noise ratio, increases the random error.

• Beam angle—as the beam angle approaches vertical, random error approaches infinity.

B. Bias error

A velocity-vector bias has a fixed magnitude and direction that either is constant or proportional to the measured velocity. Bias error is non-random and, therefore, cannot be reduced by data averaging.

Bias error due to the incorrect estimation of unmeasured velocities near the water surface and channel bottom errors of this type are called extrapolation errors. The extrapolation scheme is used to estimate cross products near the water surface and channel bed.

Suspended Sediment Concentration (SSC)

The measurement methods of SSC can be simply classified into two major categories: direct and indirect measurements. Samplers perform direct measurement, while indirect methods are based on indicators, closely correlated with the SSC (e.g., the absorption or the scatter of light, acoustic waves, lasers, etc). The Optical Backscatter Sensor (OBS) measures turbidity by emitting an infrared beam and recording infrared radiation scattered from suspended particles [34]. Optical backscatter data were converted to SSC using laboratory calibrations with sediment samples obtained at the monitoring site [47,48]. In many application, researchers use OBS to compare against the results of acoustic methods [49-51]; thus, OBS can be used as a validation method of

acoustic instruments. In this study, an OBS (INFINITY-Turbi ATU75W2-USB, JFE Advantech Ltd) was used to measure the turbidity. The specifications of this type of OBS are presented in Table 1-4.

Table 1-4 The specifications of ATU75W2-USB.

Parameter	Medium density turbidity	High density turbidity	Depth	Temperature
Principle	Infrared backscattering (LED)	Backscattering (optical fibre)	Semiconductor sensor	Thermistor
Range	0 to 1,000 FTU (Formazin calibration)	0 to 100,000 ppm (Kaolin calibration)	0 to 25 m*	-3 to 45°C
Resolution	0.03 FTU	2 ppm	0.0005 m	0.001°C
Accuracy	± 0.3 FTU or ± 2%	± 10 ppm or ± 5%	± 0.14% FS	± 0.0°C (3 to 31°C)

Many researchers use Horizontal ADCP or fixed ADCPs to measure streamflow and SSC [15] [27,28] [52-56] and some scientists use moving-boat ADCPs in river cross sections to calculate river discharge and suspended sediment flux (SSF) [57-59]. However, this method may be costly in terms of time and money. In addition, the moving-boat ADCP transects can be dangerous to perform during extreme hydrological events, such as floods and strong tides [45]. Also, this method does not provide continuous monitoring of SSF as ADCP transects are separated in time. Acoustic tomography technique is another acoustic method that is able to estimate water properties.

In contrast to the ADCPs, which use Doppler effect to measure the flow velocity and suspended particles in water, the acoustic tomography systems apply travel-time methods to measure the

various water features, such as temperature, current velocity, salinity, discharge, current direction, etc [61-64].

The Fluvial Acoustic Tomography System (FATS) has been developed by Hiroshima University since 2010 [65-67]. Although previous studies on FATS applications have highlighted advantages, two types of limits still exist. First, the imprecise determination of the angle between the flow direction and the transmission line of FATS (θ) can lead to significant errors in discharge estimation. Therefore, the utilisation of another instrument, such as an ADCP, is required to measure the angle θ accurately [50]. Second, the velocity resolution of FATS inversely depends on the length of the transmission line. In the case of choosing a short length between two transducers, the velocity resolution is low.

1.2 Purpose

In previous studies a 30-kHz FATS was used to measure river discharge, while the flow angle θ was measured by a moving-boat ADCP. The present study successfully introduces a 53-kHz FATS that permits the shorter ranges than those allowable using the 30-kHz FAT system. Moreover, the flow angle is deduced by using a cross-path configuration and a new formula based on the continuity equation.

In addition to the streamflow, the knowledge of SSC and SSF in rivers and estuaries is of interest to researchers. These physical quantities are measured by ADCPs in many applications; however,

the capability of FATS to measure the mentioned physical quantities is yet to be determined. Hence, it seems the studies on the application of FATS to measure SSC and SSF are necessary.

The thesis is divided into six parts: background and study overview (Chapter 1); the purpose of study (Chapter 2); the measurement principle of FATS (Chapters 3); field test in the Gono River (Chapter 4), Application of FATS to Ota Estuary (Chapter 5) and the Summary of this study (Chapter 6).

Chapter 1 presents background, challenges and objectives for streamflow and SSC measurements. In Chapter 2, the limitations of existing methods are described and the ability of the acoustic methods and their formulation are described. In Chapter 3, the field test of river discharge and SSF measurements by FATS in the Gono River will be discussed. Chapter 4 present the latest achievement of flow direction fluctuation measurement by FATS with the cross-path configuration method in the Gono River. Chapter 5 presents the velocity measurement by FATS in the Ota Estuary. Finally, chapter 6 presents the summary of this study.

2. Fluvial Acoustic Tomography System (FATS)

2.1 Measurement principles of FATS

Since the 1970s, scientists have attempted to investigate the influences of ocean currents, internal waves, mesoscale eddies, etc., on acoustic propagations [68-80]. The ocean acoustic tomography (OAT) technique was first proposed by Munk and Wunsch to monitor mesoscale fluctuations ocean basins [55]. After development of OAT systems, this method was used in inversions for determination of other ocean physical properties, such as mesoscale mapping, heat content, convection and temperature fields [82-85]. OAT systems employ high-powered signals with frequencies less than 1 kHz [1,2]. The Coastal Acoustic Tomography System (CATS) applies OAT to coastal waters. As CATS transmits signals at frequencies up to 10 kHz, it can be used in smaller water areas. CATS is widely used to measure tidal currents, residual currents and strait through-flow [3-6]. To use this method in shallow rivers, these systems must transmit at much higher frequencies. As a result, Fluvial Acoustic Tomography System (FATS) uses a second-generation CATS, which transmits sound at a frequency of 30 kHz. FATS measures water properties, such as temperature [59], salinity variation [8,9], flow velocity [10,11], discharge [49], flow direction [62] and SSC [51,91] in rivers and estuaries.

Sound wave propagation in aqueous media are influenced by the sound speed *C(x,y,z)* and the current velocity **u**(x,y). Hence, the travel time of sound between two acoustic stations is determined by the following integral equation [61,92]:

$$t_i^{\pm} = \oint_{\Gamma_i^{\pm}} \frac{ds}{C_0(z) + \delta C(x,y) \pm \mathbf{u}(\mathrm{x},\mathrm{y}).\mathbf{n_i}} \tag{2.1}$$

where ± represents the positive and negative direction from one transducer to another, C_0 denotes the reference sound speed, δC the deviation from the reference, **u** the velocity vector, **n** the unit vector tangent to the ray path and *s* the arc length measured along the ray path. The suffix *i* is the order number for rays traveling along various ray paths.

Travel times for the reference sound speed determined by the range-independent ray simulation are calculated as:

$$t_{0,i} = \oint_{\Gamma_{0,i}} \frac{ds}{C_0} \tag{2.2}$$

By subtracting Eq. (2.1) from Eq. (2.2), we can obtain the travel-time deviation from the reference travel times:

$$\Delta\tau_i^{\pm} = \int_{\Gamma_i^{\pm}} \frac{ds}{C_0(1+\frac{\delta C \pm \mathbf{u}.\mathbf{n}}{C_0})} - \int_{\Gamma_{o,i}} \frac{ds}{C_0} \tag{2.3}$$

Taking the Taylor expansion under the conditions of $C_0 \gg \Delta C$ and $C_0 \gg u.n$ for the first term on the right-hand side and neglecting the terms with orders higher than two, the above equation reduces to:

$$\Delta\tau_i^{\pm} \approx \int_{\Gamma_i^{\pm}} \frac{ds}{C_0}(1-\frac{\delta C \pm \mathbf{u}.\mathbf{n}}{C_0}) - \int_{\Gamma_{o,i}} \frac{ds}{C_0} \tag{2.4}$$

as the difference between the actual and reference ray paths is also sufficiently small to be two-order terms, the second Taylor expansion is applied around the reference ray path to get the following equation:

$$\Delta\tau_i^{\pm} = -\int_{\Gamma_{oi}^{\pm}} \frac{(\delta C \pm \mathbf{u}.\mathbf{n})ds}{C_0^2} + \int_{\Gamma_{oi}^{\pm}} \frac{1}{C_0}\left(1-\frac{\delta C \pm \mathbf{u}.\mathbf{n}}{C_0}\right)\Delta(ds) \approx -\int_{\Gamma_{oi}^{\pm}} \frac{(\delta C \pm \mathbf{u}.\mathbf{n})ds}{C_0^2} \tag{2.5}$$

We should notice that all the path integrations are done on the reference ray path. In Eq. (2.5), the subtraction and summation of the reciprocal travel time can separate the individual effect of current and sound speed on the travel time, which are presented in Eqs. (2.6) and (2.7), respectively.

$$\delta\tau_i^v = \Delta\tau_i^+ - \Delta\tau_i^- \approx -2\int_{\Gamma_{oi}} \frac{\mathbf{u}.\mathbf{n}}{C_0^2} \tag{2.6}$$

$$\delta\tau_i^C = \Delta\tau_i^+ - \Delta\tau_i^- \approx -2\int_{\Gamma_{oi}} \frac{\delta C}{C_0^2} ds \tag{2.7}$$

By putting the angle of ray path Γ_{0i} measured from the horizontal into $\emptyset_i$ and projecting the ray path to the horizontal plane, Eqs. (2.6) and (2.7) become:

$$\delta\tau_i^v \approx -2\int_{\Gamma_{oi}} \frac{u.cos\emptyset_i}{C_0^2}\frac{dx}{cos\emptyset_i} = -2\int_{\Gamma_{oi}} \frac{u}{C_0^2} dx \tag{2.8}$$

$$\delta\tau_i^C \approx -2\int_{\Gamma_{oi}} \frac{\delta C}{C_0^2}\frac{dx}{cos\emptyset_i} \tag{2.9}$$

The current *v* along the ray path can be assumed as the horizontal one because the vertical current is insignificant.

For the ray path shown in Figure 2-1, the vertical section-average current and sound speed are obtained for the rectangular domain surrounded by two horizontal lines passing the upper and lower turning points and two vertical lines passing the acoustic stations [65]. For the section-averaged current u_m and sound speed C_m, the ray path may be regarded as the horizontal (Figure 2-2).

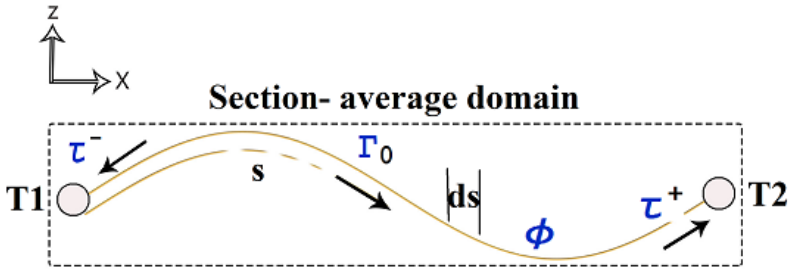

Figure 2-1 Refracted ray in the vertical section between stations T1 and T2 [65].

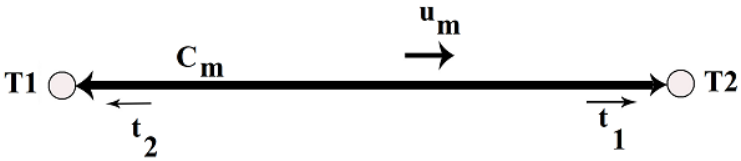

Figure 2-2 Projection to the horizontal plane [66].

The travel times are recalculated simply as Eqs. (2.10) and (2.11).

$$t_{Down} = \frac{L}{C_m + u_m} \tag{2.10}$$

$$t_{Up} = \frac{L}{C_m - u_m} \tag{2.11}$$

Solving the coupled equations above, we get:

$$\begin{cases} c_m = \dfrac{L}{t_m} \\ u_m = \dfrac{c_m^2}{2L}\Delta t \end{cases} \tag{2.12}$$

where L is the horizontal distance between the transducers, $t_m = \frac{t_{up}+t_{down}}{2}$ $t_m = \frac{t_{up}+t_{down}}{2}$

and $\Delta t = t_{up} - t_{down}$.

In the acoustically rough environment of extremely shallow waters, such as in coastal regions or rivers, a special technique for sound transmission and processing is required to prevent the sound pulse from fadeaway. To accurately identify the arrival time of a traveling acoustic signal mixed with noise in such areas, the carrier signal is phase-modulated by M-sequence [13]. Previous studies showed that modulating the carrier signal with M-sequence and taking the cross-correlation of the signal received with it proved to be enormously efficient in shallow waters. M-sequence is a type of pseudorandom signal by which the phase shift of π in the carrier is generated with irregular time intervals [94,95].

Figure 2-3 shows a typical example of M-sequence with the time series of the original signal and its auto-correlation coefficient. M-sequence has two kinds of time scales, the period (T_p) and the width of one digit (T_r), which is the time resolution of the system for multiple arrivals.

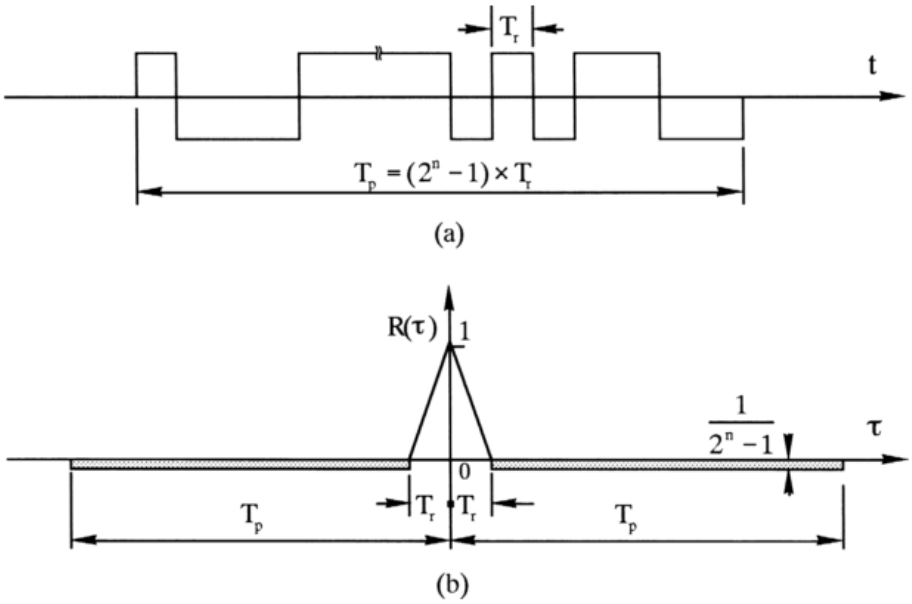

Figure 2-3 A typical example of M-sequence. (a) A period of M-sequence. (b) Auto-correlation coefficient of M-sequence [69].

After the auto-correlation procedure, the signal-to-noise ratio (SNR) of modulating transmitted signal escalates by $(2^n - 1)$ times for the M-sequence of n'th order. The improved rate of the SNR is called the processing gain (G_p).

When two acoustic rays with same intensities arrive successively within an interval shorter than T_r, the cross-correlation pattern of the rays will overlap (Figure 2-4 a). If two acoustic rays with

different intensities arrive successively, individual correlation peaks may be detectable even for the overlapped arrival because of the difference of the peak height.

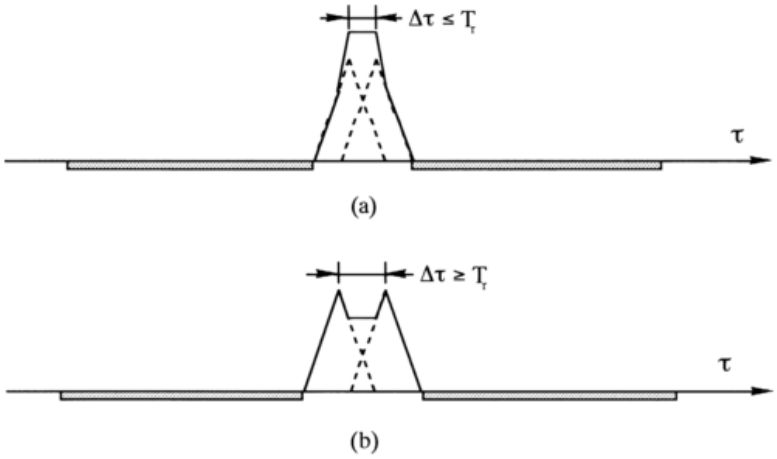

Figure 2-4 Sketch showing the resolution of M-sequence. (a) Case with auto-correlation peaks spaced less than Tr. (b) Case with auto-correlation peaks spaced greater than Tr [69].

The accuracy of travel time measurement, T_a, depends on the time resolution of the system (T_r) and the SNR and can be expressed by [70]:

$$T_a = \frac{T_r}{\sqrt{10^{0.1\,SNR}}} \tag{2.13}$$

The measurement principle of the FATS is the same as that used in an Acoustic Velocity Meter (AVM), whereby the range-averaged velocity along the transmission line is calculated by using the "travel-time method". However, the FATS transmits multi-ray paths throughout the cross section of river, hence it can measure the cross-sectional averaged velocity.

FATS utilises the travel time method and measures flow velocity along the sound ray paths (u) of two acoustic stations (Figure 2-5) [65,98]. Hence, the cross-sectional averaged velocity (v) can be given by Eq. (2.14).

$$v = \frac{u_m}{\cos\theta} \tag{2.14}$$

where θ is the angle between the ray path and the stream line. The determination of the angle θ requires extra devices such as moving-boat ADCP, which measures flow direction [50].

The continuous measurement of θ is difficult. If stream gauges are available in the study area, θ can be deduced by establishing non-linear fitting model to streamflow obtained from the RC (Q_{RC}) method, which are extracted from stream gauges at the gauging station, the mean water elevation *D(m)* measured by a water level logger and the mean flow velocity through the ray path (u) measured by FATS.

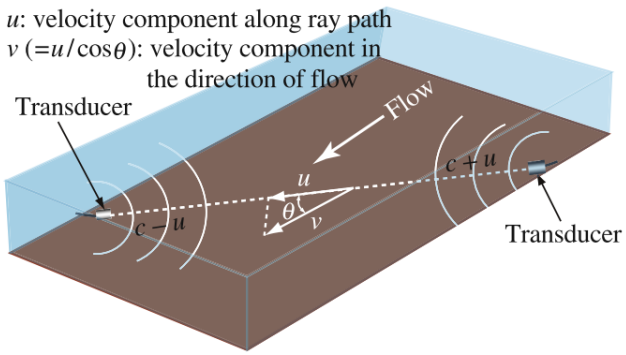

Figure 2-5 The angle of sound ray path and flow direction [48].

Assuming that the water surface profile between both transducers is linear, streamflow (Q) can be deduced by the following equation:

$$Q = (Lh_m - A_B)\ \tan\theta \times u \tag{2.15}$$

where L is the horizontal distance between the transducers and h_m is the mean water elevation. A_B is the function of bed level as (Fig.3):

$$A_{B=} \int_0^L Z_b\,(y)dy \tag{2.16}$$

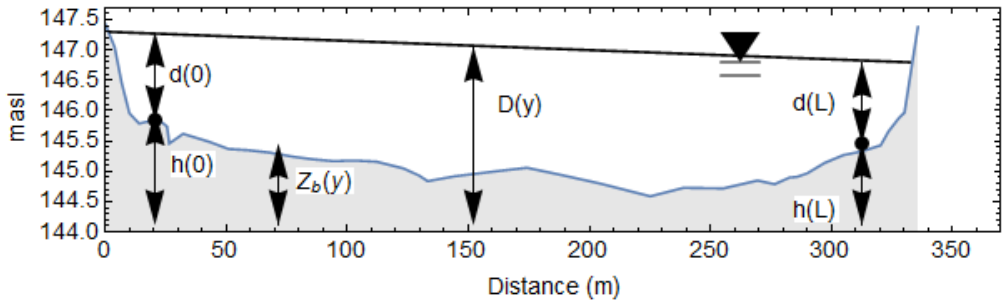

Figure 2-6 Cross section of river and the position of two stations

2.2 Error structure in the streamflow measurements by FATS

Kawanisi et al. [18] showed that the error structure of FATS measurement is a function of water depth, river bathymetry, the section-average-velocity component along the transmission line and the angle between the transmission line and the stream axis.

$$\delta Q = \delta Q_{h_m} + \delta Q_{A_B} + \delta Q_{u_m} + \delta Q_\theta \tag{2.17}$$
$$= \frac{\partial Q}{\partial h_m}\delta h_m + \frac{\partial Q}{\partial A_B}\delta A_B + \frac{\partial Q}{\partial u_m}\delta u_m + \frac{\partial Q}{\partial \theta}\delta\theta$$

Thus the relative error of streamflow (Q) can be presented as Eq.(2.18):

$$\frac{\delta Q}{Q} = \frac{\delta Q_{u_m}}{Q} + \frac{\delta Q_A}{Q} + \frac{\delta Q_\theta}{Q} \tag{2.18}$$
$$= \frac{\delta h_m/h_m}{1 - A_B/(Lh_m)} + \frac{\delta A_B/A_B}{1 - L\,h_m/A_B} + \frac{\delta u_m}{u_m} + \frac{\delta\theta}{\cos\theta\,\sin\theta\,sin}$$
$$= \frac{\delta h_m}{h_m - Z_b} + \frac{\delta A_B}{L(Z_b - h_m)} + \frac{\delta u_m}{u_m} + \frac{\delta\theta}{\cos\theta\,\sin\theta\,sin}$$
$$= \frac{\delta h_m}{d_m} - \frac{\delta Z_{Bm}}{d_m} + \frac{\delta u_m}{u_m} + \frac{\delta\theta}{\cos\theta\,\sin\theta\,sin}$$

where L is the horizontal distance between two acoustic stations, d_m is the mean water depth and Z_{Bm} is the mean bed level. Consequently, in the case of shallow depths, accurate river stage and bed level observations are required to minimize the first error and second terms. Besides, the second error term is induced by temporal variations in the mean bed level.

The $(\frac{\delta Q_{um}}{Q})$ is uncertainty due to the FATS velocity, and the last term $(\frac{\delta Q_{\theta}}{Q})$ is due to the angle between the transmission line and the stream axis. The results of error analysis will be discussed in the subsection 4-8.

3. Measurements of Suspended Sediment Concentration and Streamflow

3.1 Experiment site and deployment

The Japanese archipelago lies between 24° and 46°N. The islands of Japan have several different climatic regions ranging from severe cold to subtropical. Miyoshi City is located in the cool-temperate region where the average annual temperature varies from 8.5°C to 19.4°C and the average precipitation is 1492 mm. Field measurements were carried out in a section of the Gono River, located in Miyoshi City. The length of the Gono River is approximately 194 km. The Basen River and Saijo River are the two main tributaries of the Gono River. These rivers meet approximately 3 km upstream from the observation site (Figure 3-1 (a)). A 115-m wide, straight reach of the river was selected for the location of the transducers. The bed slope surrounding the observation site is 0.11%. The bed in the observation site is mainly composed of gravel and boulders. The mean water depth is about 0.55 m and 1 m under low-flow and high-flow conditions, respectively. The annual mean discharge at the Ozekiyama gauging station, located 1.1 km upstream of the observation site, is around 73 m^3/s.

Measurements of flow velocity, river discharge and cross-sectional average SSC <SSC>, were done by FATS in this shallow river over one month. The reciprocal sound transmission by FATS was performed between the two acoustic stations, located on both sides of the river in March 2015

(Figure 3-1). The FATS was equipped with two 30-kHz broadband transducers with horizontally omnidirectional and vertically hemispherical beam patterns. The horizontal distance between the two stations was 294.629 m and the angle between the ray path and stream direction θ was 17°. The acoustic pulses were triggered by a GPS clock and were transmitted simultaneously from both transducers every 30 s. The water level was measured every 10 min by water-level loggers attached to the S1 and S2 transducers. A barometer on the riverbank was used to record atmospheric pressure. The accuracy of the water-level sensors and the barometer was ± 5 and ± 3 mm, respectively.

Between March 26th and 28th a total of 23 water samples of 1 L were taken from under the Iwai Bridge every 80 min to examine SSC and grain size distributions of suspended sediments (Figure 3-1(a)). The grain size of the water samples was analysed by the laser diffraction and scattering method (SALD-2000J, SHIMAZU Ltd). To measure the SSC profile continuously, an uplooking 2 MHz ADCP was mounted on the bed near the ray path of FATS. Data was collected at a 1.0 Hz sampling rate and 10 cm cell size. A Compact CTD (Conductivity- Temperature- Depth meter) (accuracy: ± 0.3 FTU) developed by Alec Electronics was used to check turbidity profiles at four points (P1 to P4, from the left side respectively), the CTD casted was from the Iwai Bridge every 20 minutes in 0.1m depth-triggered mode.

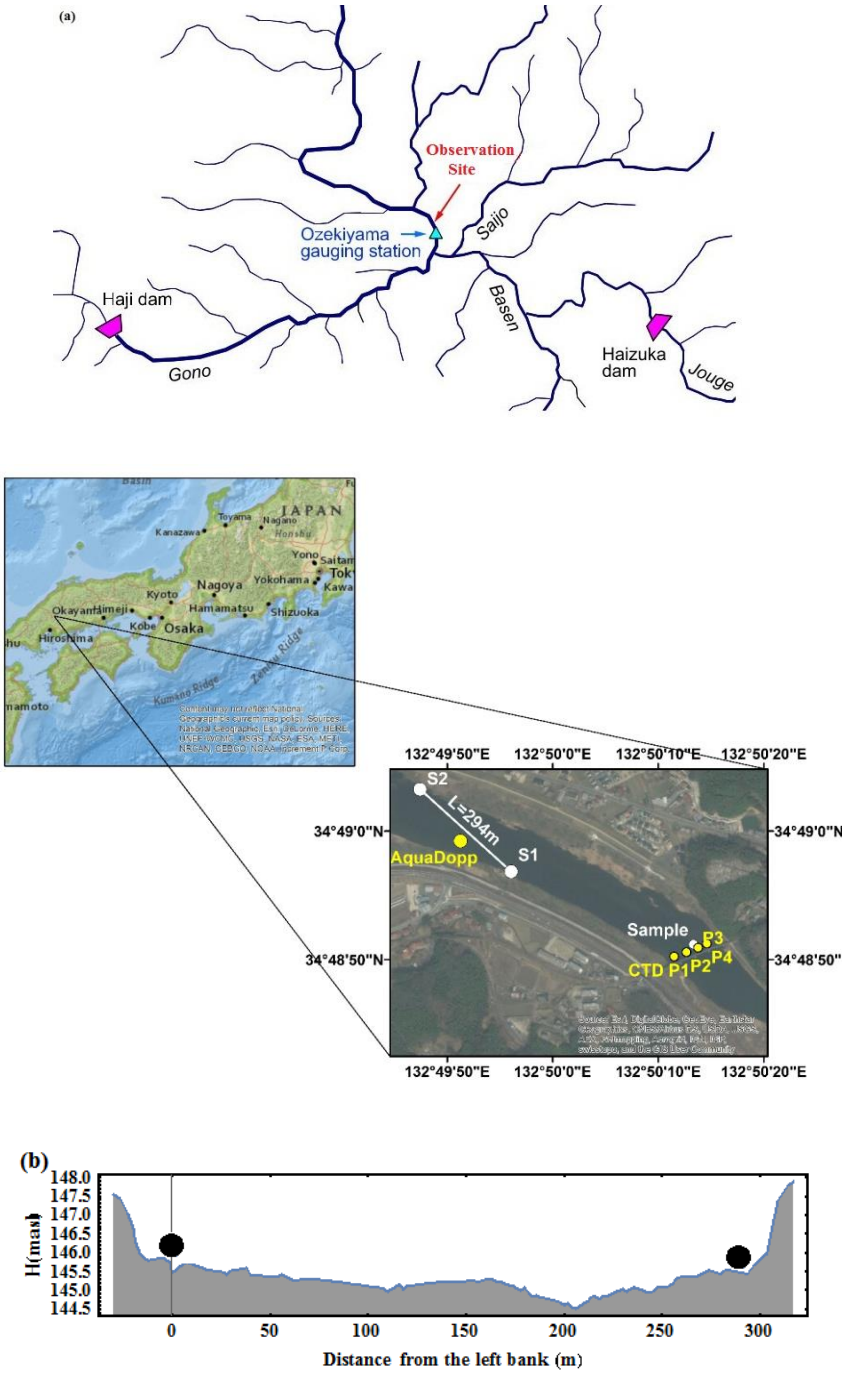

Figure 3-1 (a) Study area and experimental site; (b) Oblique cross section of river and the position of two stations (black points denote the transducers positions).

3.2 Acoustic measurements of suspended sediment concentration (SSC)

Since the acoustic technique is an indirect method to estimate SSC, some processes are needed to convert the received signals to the SSC values. One of the most important terms in using acoustic methods is to understand sound attenuation in fluid media. Below is a brief overview of the determination of the sound attenuation coefficient and the basics of the acoustic inversion algorithm for measuring the SSC.

3.2.1 Sound attenuation due to SSC

Sound is exponentially attenuated with distance from a source transmitter [72]. The attenuation coefficient is a function of various parameters, including water characteristics such as temperature, pressure, salinity and the suspended sediment properties (e.g., size, shape, mineralogy and SSC) [73]. The total sound attenuation coefficient (α) is bipartite: the attenuations by water (α_w) and by suspended sediments (α_s). The coefficient (α_w) is easily found in acoustic communities [74]. As it can be seen in Eq. (3.1), the attenuation by sediments, α_s, is determined by the SSC in the sensing range (R) and two sound absorption components of the scattering loss (ξ_s) and the viscous absorption (ξ_v) [73]:

$$\alpha_s = \frac{1}{R}\int_0^R (\xi_s + \xi_v) SSC(r) dr \tag{3.1}$$

Using Urick's expression for the viscous absorption coefficient and assuming all particles are the same size, the attenuation coefficient due to viscous absorption may be expressed as:

$$\xi_v = (10loge^2)\left(\frac{\epsilon k(\sigma-1)^2}{2}\left[\frac{s}{s^2+(\sigma+\delta)^2}\right]\right)\frac{dB}{m} \tag{3.2}$$

Where

$\delta = \frac{1}{2}\left[1+\frac{9}{2\beta a}\right]$, $s = \frac{9}{4\beta a}\left[1+\frac{1}{\beta a}\right]$, $\sigma = {\rho_s}/{\rho_0}$, $\beta = \sqrt{{\omega}/{2\upsilon}}$ is the reciprocal of the viscous skin depth; ρ_s and ρ_0 are the densities of the particulate and water, respectively; υ is the kinematic viscosity of the ambient fluid; ϵ is the volume concentration of the particulate; a is the particle radius; k is the acoustic wave number and ω is the angular frequency of the incident pressure wave. The first term on the right-hand side of Eq. (3.2) is a constant that converts attenuation from Nepers/m to dB/m.

The attenuation constant due to the scattering loss (ξ_s) can be estimated using the following expression [75][73]:

$$\xi_s = \frac{1}{\rho_s a_s}\left[\frac{\gamma(ka_s)^4}{1+(ka_s)^2+\frac{4}{3}\gamma(ka_s)^4}\right] \tag{3.3}$$

where k is the acoustic wavenumber and ρ_s and a_s are the density and equivalent sphere radius of suspended particles, respectively. For quartz particles, $\gamma = 0.18$.

3.2.2 SSC estimation using backscatter of ADCP

ADCPs, as the most well-known devices, are widely used in many applications [103-105]. Unlike the automatic measurements of flow velocities and river discharges [11,30] produced by the use of existence software, the ADCP cannot automatically measure the SSC and needs an inversion model to convert the recorded series of backscatter data into parameters of suspended sediment concentration.

In this study SSC will be calculated using the following equation [78]:

$$(10\log(SSC) - 2(\alpha_s + \alpha_w)R - 20\log(\psi R) = K_c E + C \tag{3.4}$$

where E is echo level (in counts), R is the distance between the transducer and measurement volume, α_w and α_s are attenuation coefficients due to water and suspended sediment, respectively and Kc and C are signal calibration coefficients. Close to the transducer, the assumption of spherical spreading of the signal is no longer valid, therefore the coefficient ψ is used in Eq. (3.4) to distinguish between near and far transducer fields [79].

It should be noted that it is impossible to directly estimate the SSC profile using Eq. (3.4) because α_s is also a function of SSC. However, through the iterative calculation with known calibration

coefficients, SSC and α_s at each cell can be sequentially computed either by implicit or explicit approaches [22,108]. More details on signal inversion can be found in [22,109]. Here, we employ an explicit approach to derive unknown parameters.

3.2.3 SSC estimation using FATS

FATS uses two acoustic stations on the both sides of river, so it can measure SSC through the whole cross section of river, which is the cross-sectional average SSC <SSC> (3.5). <SSC> is estimated from the SNR of the FATS using a simplified sonar equation [38] [110]:

$$< SSC > (t) = -\frac{1}{L\xi_v}\big(SNR(t) - SNR(t_0)\big) + < SSC > (t_0) \tag{3.5}$$

where L is the ray path length, ξ_v is the viscous absorption coefficient, *SNR* is the signal-to-noise ratio, t_0 is the base time of calculation and t is the elapsed time.

3.3 Streamflow

The angle between the sound ray path of FATS and the flow direction (θ), shown in Eq. (2.14), was determined by nonlinear regression analysis of FATS velocity (u) and the mean water elevation (D_m) obtained from water level loggers attach to the transducers of FATS against the hourly discharge data from the well-established RC method, which was conducted using data from the Ozekiyama gauging station. The result of analysis yielded a value of 19.34° for θ. The 95% confidence interval for θ ranged between 19.25° and 20.48°. In order to validate the proposed

approach, the fluctuations of flow direction changes were measured by the ADCP. As illustrated in Figure 3-2, the flow direction varies between 19 and 19.4° before arrival of the first dam flush. Subsequently, an increment is observed for the passing of the first dam flush between 22:00 and 01:00. After the passing, the angle θ gradually decreased to 19° again. When the second dam flush is passing, the angle θ slowly increased from 18.8° to 20.3° degrees between 13:00 and 18:30. The comparison of θ acquired by ADCP and that from the regression model reveals a difference less than 0.13°. This confirms the efficiency of the proposed approach as an alternative methodology in the absence of suitable equipment. As shown in Figure 3-2, the stream direction is 19° during low-flow conditions and changes by approximately one degree according to the velocity increment.

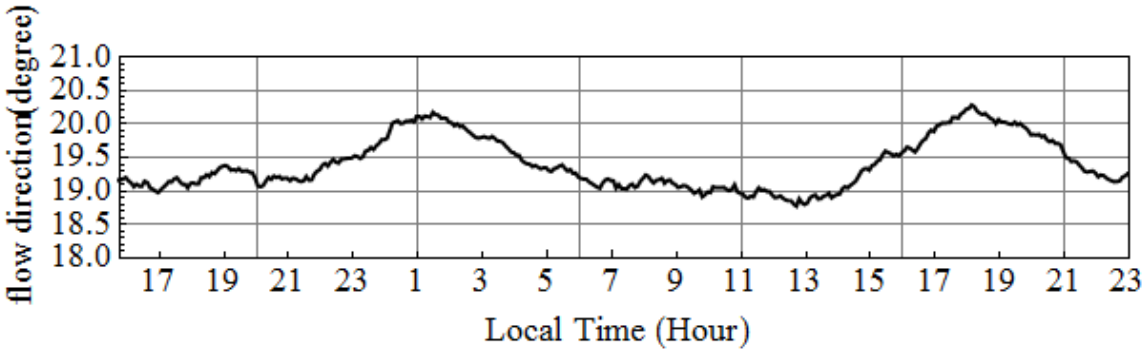

Figure 3-2 Flow direction fluctuations measured by ADCP.

The mean flow velocity (v_m) can be calculated using u and θ as shown in Figure 3-3. The mean velocity varies between 0.6 m/s and 1.6 m/s. The three peaks in the flow velocity record are due

to the precipitation and the velocity increments on the 27th of March as a result of the dam flushing, which reached up to the 1 m/s.

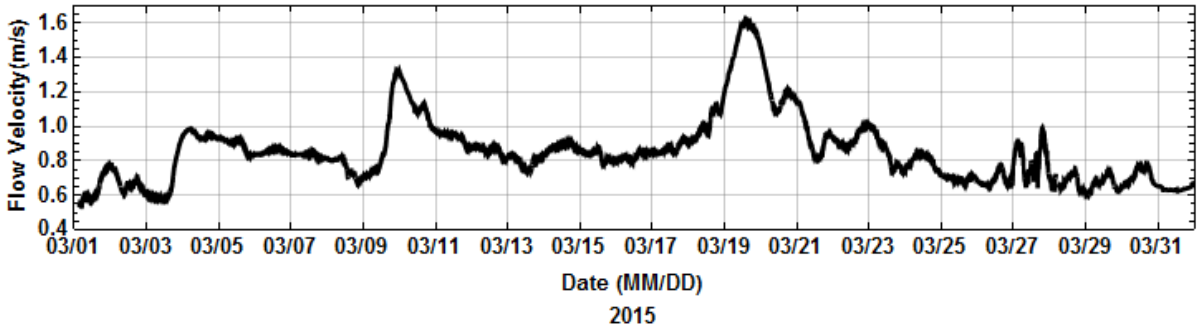

Figure 3-3 Flow velocity measurement by FATS.

The temporal variation of water level at the Ozekiyama gauging station is illustrated in Figure 3-4 (a). On the 10th and 20th of March, the water level increased because of heavy precipitation. The increments of water level on the 27th of March are a result of dam flushing. Using mean velocity and cross-sectional area, water discharge was calculated. The comparision of FATS (black line) and the RC estimates (blue line) for Ozekiyama gage station shown in Figure 3-4 (b). This continuous monitoring shows the efficiency of FATS to measure river discharge with minimum effort. Other acoustic methods, such as moving-boat ADCP collects velocity samples and discharge separately in time (definitely not continuously) [50] and can be dangerous during extreme hydrological events such as a flood [45]; H-ADCP (Horizontal ADCP) in a fixed location needs extra methods to calculate river discharge. As shown in Figure 3-4 (b), the river discharge is about 60 m^3/s in the low flow condition and because of the high precipitation, the streamflow

reaches 140 m^3/s, 220 m^3/s and 270 m^3/s on 4th, 10th and the 20th of March, respectively. The flushing of the Haizuka and Haji dams cause the sharp increment in the river discharge that reaches 130 m^3/s and 150 m^3/s, respectively.

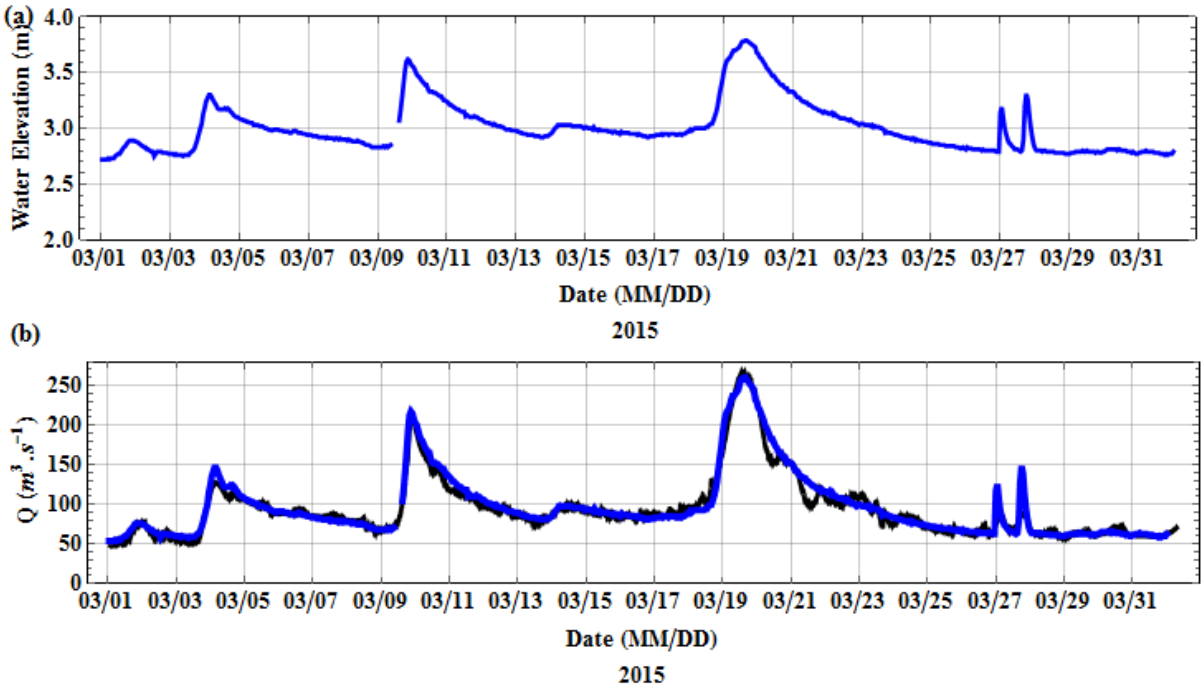

Figure 3-4 (a) Water level variation at Ozekiyama gage station; (b) discharge of FATS (black line) and discharge of RC (blue line).

According to Figure 3-5 (a), the relative difference between the RC and FATS estimation is less than ± 20%. Root-mean-square of the residuals (RMSR) was 9.42 m^3/s. As well, there is a quadratic relationship between the streamflow and water levels for the parabolic river cross-

sections. Hence, the high correlation of the root value of discharge estimation of FATS and the Ozekiyama water level with determination coefficient (R^2=0.97) is observed (Figure 3-5 (b)).

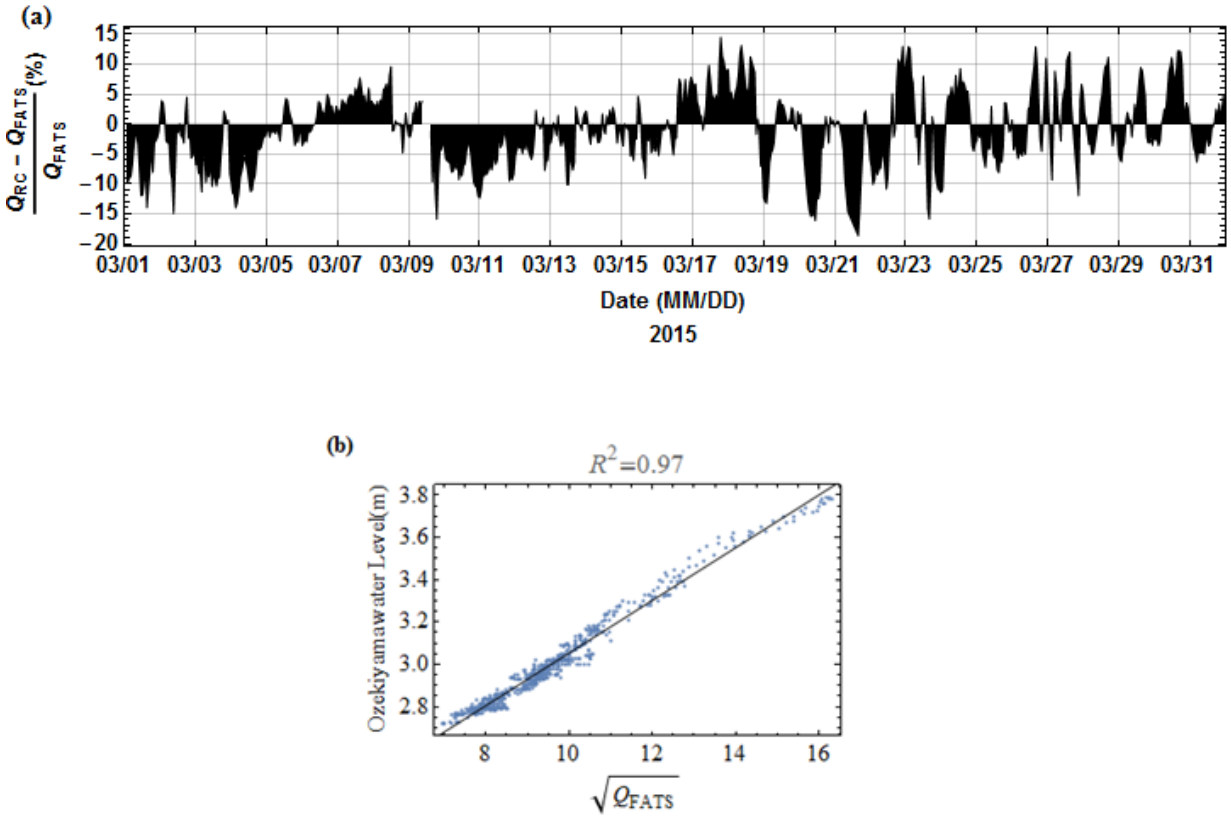

Figure 3-5 (a) Relative difference between RC and FATS estimation of streamflow; (b) the correlation of water level in Ozekiyama gauging station and root of streamflow estimation of FATS.

3.4 SSC

3.4.1 Sound absorption

Sound absorption by particles is shown in Figure 3-6. The horizontal axes are the particle radius in μm and the vertical axes are the viscous attenuation (dotted line), attenuation due to the scattering loss (dashed line) and the sum of two terms (green line). In this study, the mean particle radius obtained by samples was 16 μm, thus attenuation due to scattering loss is insignificant and can be ignored. As was mentioned previously, sound attenuation is a function of frequency. According to the Figure 3-6, for the same particle size (as = 16 μm), the viscous attenuation is 0.026 and 0.24 dB m^2/kg for FATS and ADCP, respectively. This difference determines the measuring range of acoustic instruments and it means that with an increment in the SSC, the acoustical signals become attenuated by the suspended particles and produce inadequate results.

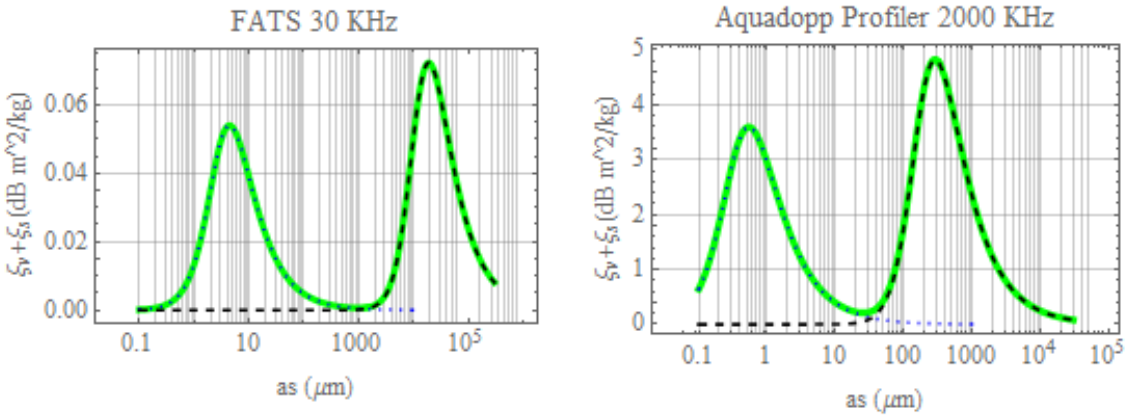

Figure 3-6 Sound absorption coefficient of FATS and ADCP profiler.

3.4.2 Temporal variations of <SSC> and SSC flux using FATS

During the observation period in low-flow conditions (Q< 60 m^3/s), the <SSC> does not exceed 0.02 kg/m^3. These low <SSC> are observed on the 3rd and 9th of March, before the heavy

precipitation events. The <SSC> is also low before the dam flushes on the 27th of March. The maximum <SSC> reached up to the 0.1 kg/m^3. SSF can be obtained as the product of <SSC> and the river discharge. A moving average was taken to remove existing spikes. As shown in Figure 3-7 (b), during the heavy rains on the 10th and 19th of March and during the passing of the dam-flush waves, the river transferred 15, 23, 9 and 8 kg/s of suspended sediments, respectively. The Haizuka dam is located on a steep river reach, whereas the Haji dam is located in the mild reach of the river. Hence, the Haizuka dam flush washed the deposited sediments in the its path, consequently, the <SSC> and SSF was larger than that of Haji dam flush (Figure 3-7 (a), (b)).

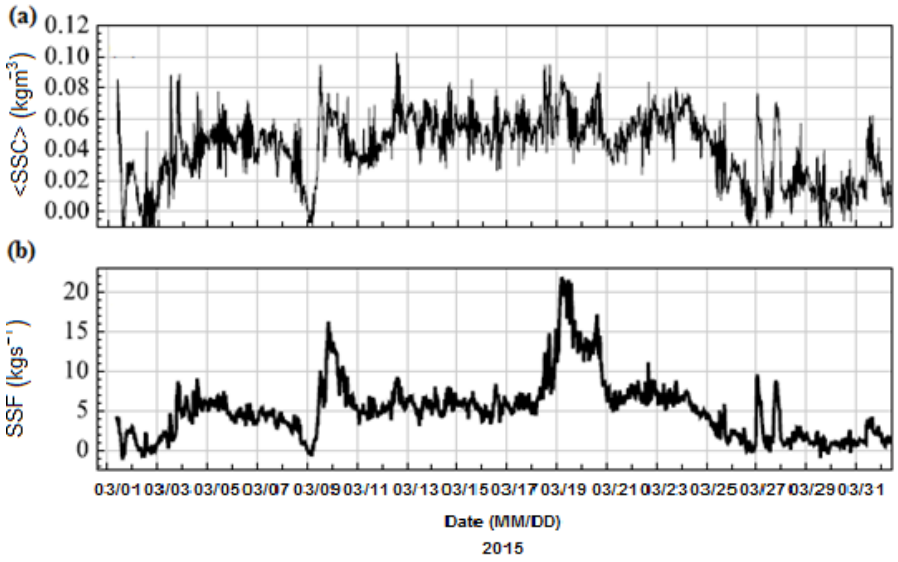

Figure 3-7 (a) cross-sectional <SSC>; (b) estimation of SSC flux using FATS.

The period of the dam flush discharges was chosen to validate the SSC estimation of FATS by other methods, which will be discussed in the next section. An interesting point of this result was

that although the second dam flush discharge was greater than the first (Figure 3-4 (b)), the SSF in the second dam flush was smaller than that in the first dam flush (Figure 3-7 (b)).

3.5 Validation results of <SSC> and streamflow

The dam flush period in March was selected to validate the result of <SSC> estimated by FATS. The Haizuka and Haji dams, which are located around 26 and 40.2 km in the upstream of study area, flushed their storages on the 26th and 27th of March 2015, respectively **(**Figure 3-1**)**. The arrival times of dam flushes at the study area were 01:00 and 18:30 on the 27th of March 2015, respectively. Hence, the validation period was chosen from 26th to 28th of March.

Thirteen water samples of 1 L were taken at the Iwai Bridge to measure SSC and grain size distributions of suspended sediments **(**Figure 3-1**)**. The grain size of the water samples was analysed by the laser diffraction and scattering method (SALD-2000J, SHIMAZU Ltd). To continuously measure the SSC profile, an up looking ADCP (Aquadopp Profiler) was installed upwardly on the riverbed near the left side station. The data were collected at a sampling rate of 1/300 Hz and cell size of 0.1 m. A CTD (accuracy: ± 0.3 FTU), operating in 0.1m depth-triggered mode, was used to check turbidity profiles at four points (P1 to P4) from the Iwai Bridge every 20 min **(**Figure 3-1**)**.

3.5.1Turbidity

Sediment concentrations determined from water samples were used to convert the turbidities of OBS to SSC (Figure 3-8). The high correlation between SSCs from water samples and turbidities of OBS (R^2 = 0.97) confirms that the OBS measurements can be used as a reliable method to validate the results of acoustic methods.

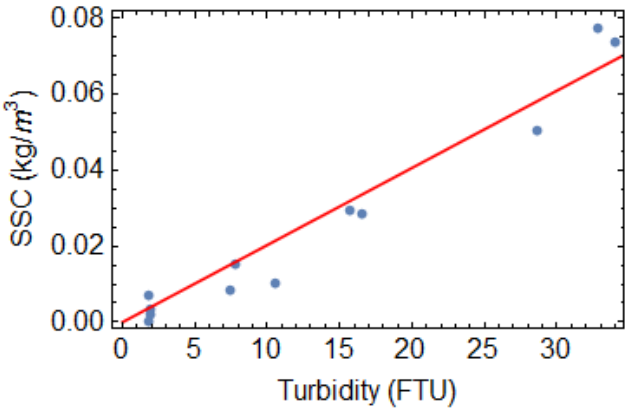

Figure 3-8 Calibration curve of OBS.

The turbidity profile in the centre of river (P3) is shown in **(**Figure 3-9**)**. When the river is in a normal state, the turbidity magnitude was almost constant with respect to the depth and had a value less than 5 FTU. After the arrival of the dam-flush waves, the turbidity increases up to 47 and 42 FTU near the riverbed at depths of 1.4 and 1.6 m, respectively (Figure 3-9**)**. Figure 3-10 shows the depth-averaged turbidity obtained for all points. As shown in this figure**,** all four points in the river cross section show almost the same values, i.e, turbidity has almost the same value throughout the river cross section.

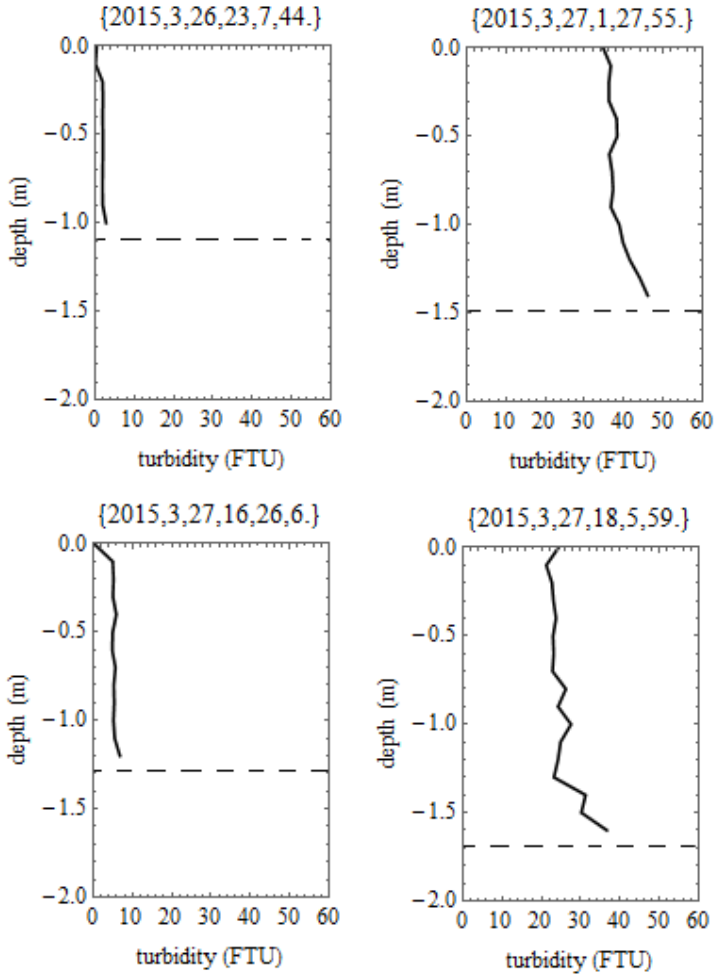

Figure 3-9 Turbidity profile before and after the dam flushes (dashed line denotes the riverbed).

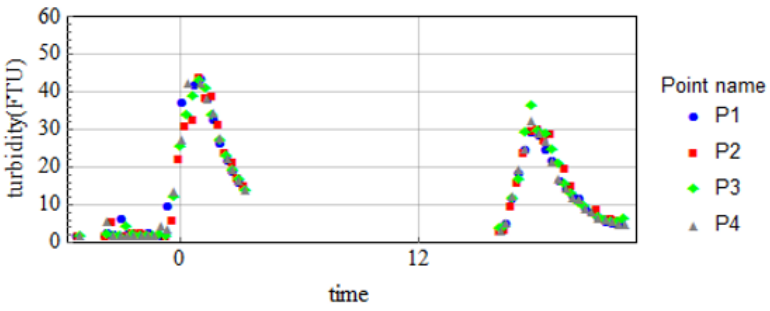

Figure 3-10 Depth-averaged turbidity from OBS measurements.

3.5.2 SSC estimated by ADCP

SSC was estimated at three different heights from backscatter data of ADCP. As shown in Figure 3-11 (a), SSC increases with respect to the depth similar to the results of SSC profiles obtained by OBS. The maximum SSC of 0.08 kg/m^3 is observed at 0.2 m above the riverbed. Figure 3-11 (b) shows the comparison of depth-averaged SSC measured by ADCP (red line) against OBS (black points) [111-115] and R^2 of 0.96 was observed. At low concentrations, both methods show almost the same values of SSC and during the first peak, OBS absolutely confirms the ADCP results. However, for the second peak although the ADCP overlays the OBS measurement in the increment period, it overestimates during the decrement period of SSC.

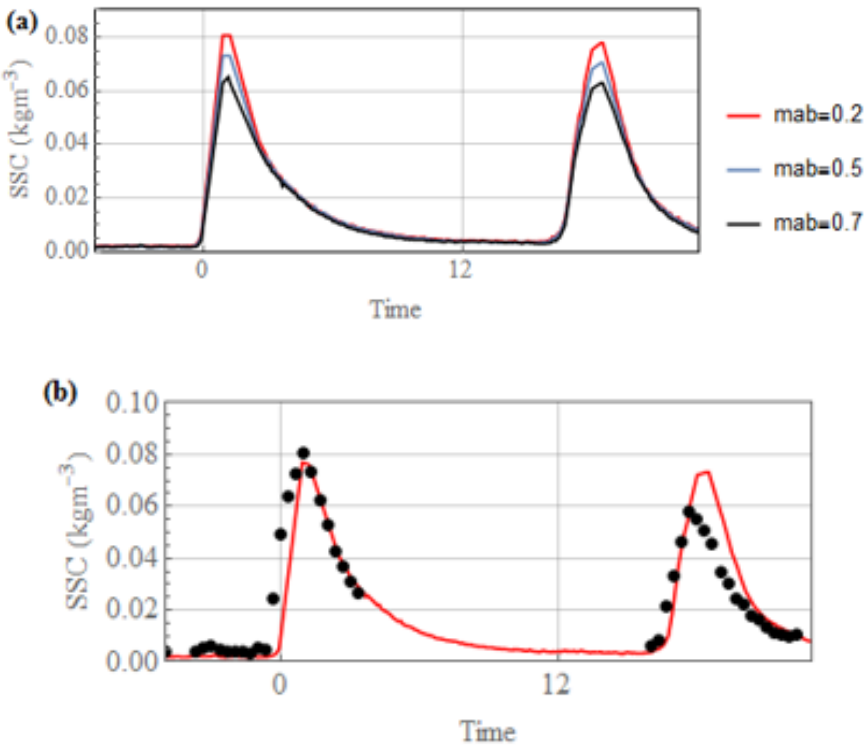

Figure 3-11 (a) SSC from ADCP at three heights above the riverbed; (b) depth-averaged SSC by ADCP (red line) and OBS (black points).

3.5.3 Comparison between <SSC> and OBS estimates

The fluctuations of SNR for both stations are shown in Figure 3-12. Before the arrival of the waves, the amount of suspended sediment was low and SNRs of the received signals are 25 dB and 35 dB at stations S1 and S2, respectively. The observed sharp drop at the stations is due to the dam-flush discharges. Prolongation of the dropped SNR during the passage of the second wave is due to the disturbance of weeds attached to the S2 station, which caused error in the velocity and <SSC> measurements.

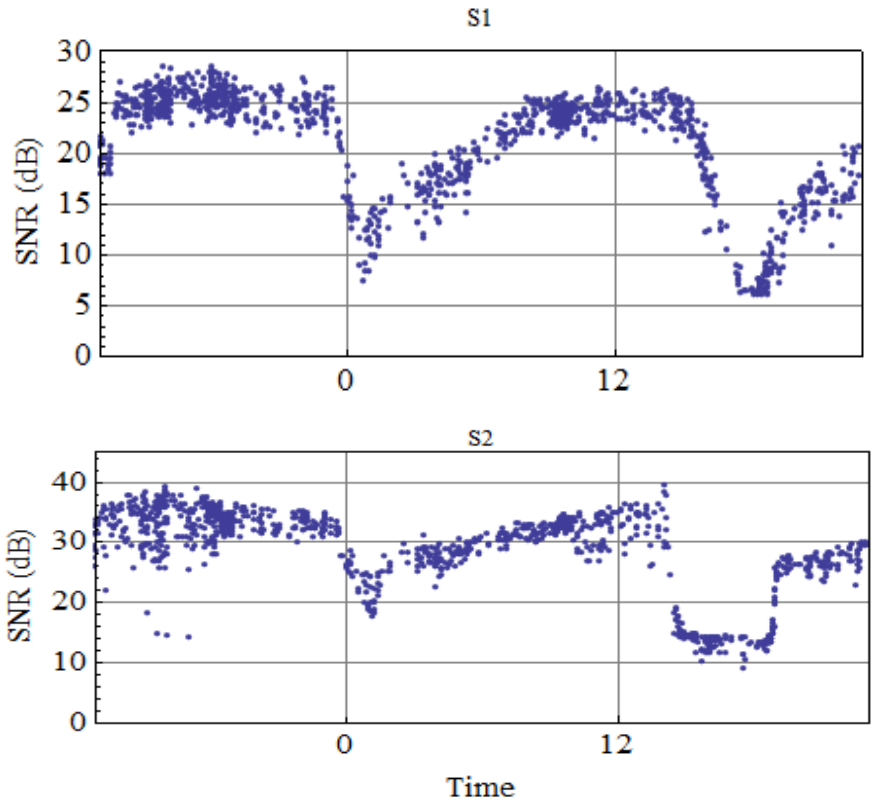

Figure 3-12 SNR fluctuations at stations S1 and S2.

It is clear that FATS successfully measured the mean flow velocity continually, however a perturbation of arrival time of signals was observed at the downstream station (S2), which caused a gap in the flow velocity measurements during the second dam-flush wave. In-situ investigations reported that weed accumulation was the reason behind the perturbation. The flushed flow from the Haji dam carried large amount of weeds that got stuck over the S2 transducer (Figure 3-13).

Consequently, this prevented the transmission and receiving signals. Therefore, this was probably the reason for the short missing period of data at the arrival time of second dam-flush wave.

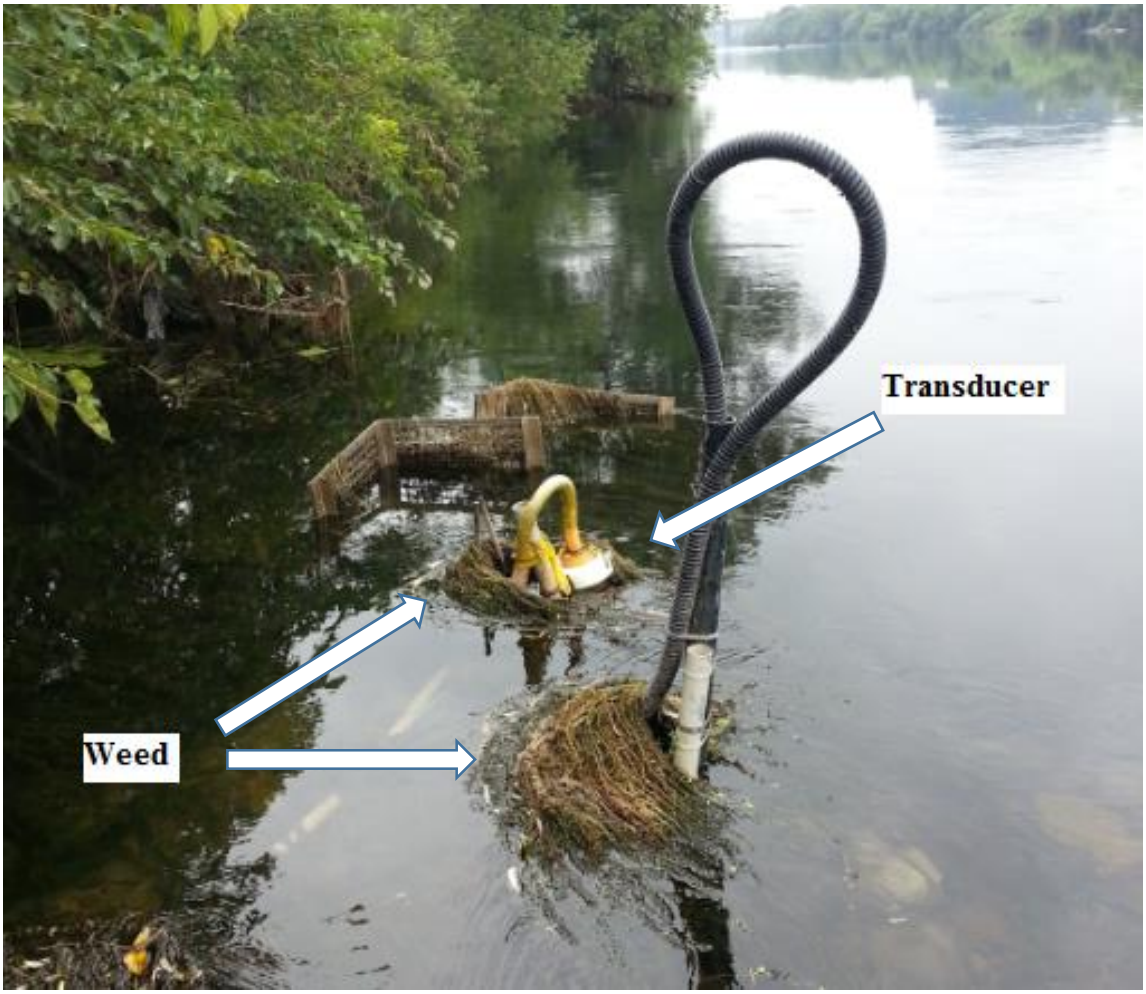

Figure 3-13 The transducer covered with a tangle of weed at the S2 station.

According to Eq. (3.5), the cross-sectional average SSC <SSC> can be deduced from the SNR of FATS. The <SSC> was compared to the OBS measurement **(**Figure 3-14**)**. It can be seen that the OBS measurements absolutely confirm the estimate of FATS during the increment periods, however during the decrement, the reduction of estimated <SSC> is smaller than the SSC measured by OBS. For the second flushing, the significant amounts of weed that accumulated over the transducer at S2 disturbed the transducer functionality. Thus, the weed may have led to the overestimation in <SSC> **(**Figure 3-14**)**. The results show that the <SSC> was less than 0.01 kg/m^3 during normal discharge but during dam-flush discharges <SSC> increased dramatically and reached 0.08 kg/m^3 and 0.06kg/m^3 after the flushing of the Haizuka and Haji dams, respectively. It was also observed that the Haizuka dam flush carried more suspended sediment than the Haji dam flush.

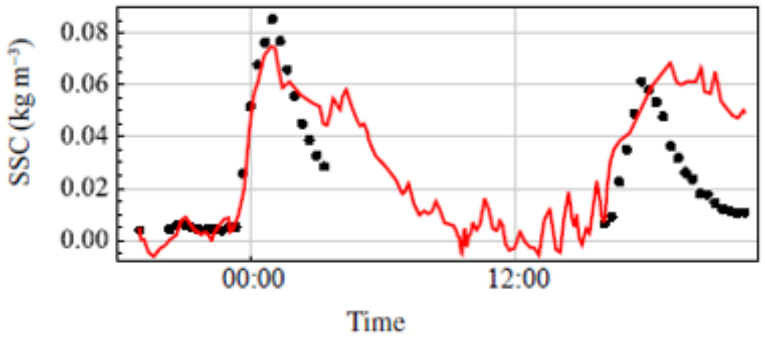

Figure 3-14 <SSC> estimated by FATS (red line) and OBS (black points).

3.6 Conclusion

Measurement of streamflow and SSF over a one-month period was performed by FATS, which is a new acoustic instrument. In the previous studies, other instruments such as ADCPs or a different set of FATS were needed to measure the flow angle (θ); however, in this study a regression analysis was proposed to estimate θ. The result of θ estimation was 19.34°. A deployed ADCP also measured the flow direction changes that confirmed the efficiency of proposed method with a difference less than 0.13°.

The streamflow measured by FATS varied from 60 m^3/s to 270 m^3/s in March 2015. The streamflow results were compared to the RC estimates. The root-mean-square of the residuals (RMSR) between FATS and RC was 9.42 m^3/s.

The SSC comparison between FATS measurement and other methods including OBS and ADCP during a dam flush operations, showed the capability of FATS to measure suspended sediment concentration. It also concluded that unlike the other two methods, FATS can estimate the suspended sediment flux in a cross-section of river. However, it was observed that the existence of weeds can cause the large errors in FATS measurement. The maximum SSF that was transferred in the river was 23 kg/s on 19th of March 2015 and the amount of SSF due to the Haizuka and Haji dams flushing were 10 kg/s and 8 kg/s, respectively.

4. Streamflow measurement using cross-path configuration

4.1 Experiment site and deployment

Field measurements were carried out in a section of the Gono River, located in Miyoshi City. The reciprocal sound transmission by FATS was performed between four acoustic stations located on both sides of the river during the period of January 13th to 20th, 2016. The air temperature ranged from 4.6 °C to 22.1°C and there was precipitation on the 18th and 19th. Stations 1 and 2 were equipped with two 30-kHz broadband transducers, whereas Stations 3 and 4 were equipped with two 53-kHz transducers (Figure 4-1 (b)).

The horizontal distances between the 30-kHz and 53-kHz systems were 294.629 m and 161.167 m, respectively and the angle between the two lines (∅) was 67° (Figure 4-2 (a)). The acoustic pulses were triggered by a GPS clock and were transmitted simultaneously every 30 s and 60 s for the 30-kHz and 53-kHz systems, respectively. The water temperature and water level were measured every 10 min by water level loggers attached to all transducers. The accuracy of the water level sensors was ± 5 mm. The river bathymetry along the transmission lines of the 53-kHz and 30-kHz transducers was surveyed by a Teledyne RDI StreamPro ADCP and is shown in Figure 4-2 (a). As the drift of the transducers in the river can cause significant error in the measurements, all transducers attached to heavy stands. Moreover, several anchors fixed the stands and cables on the riverbed (Figure 4-2 (b)).

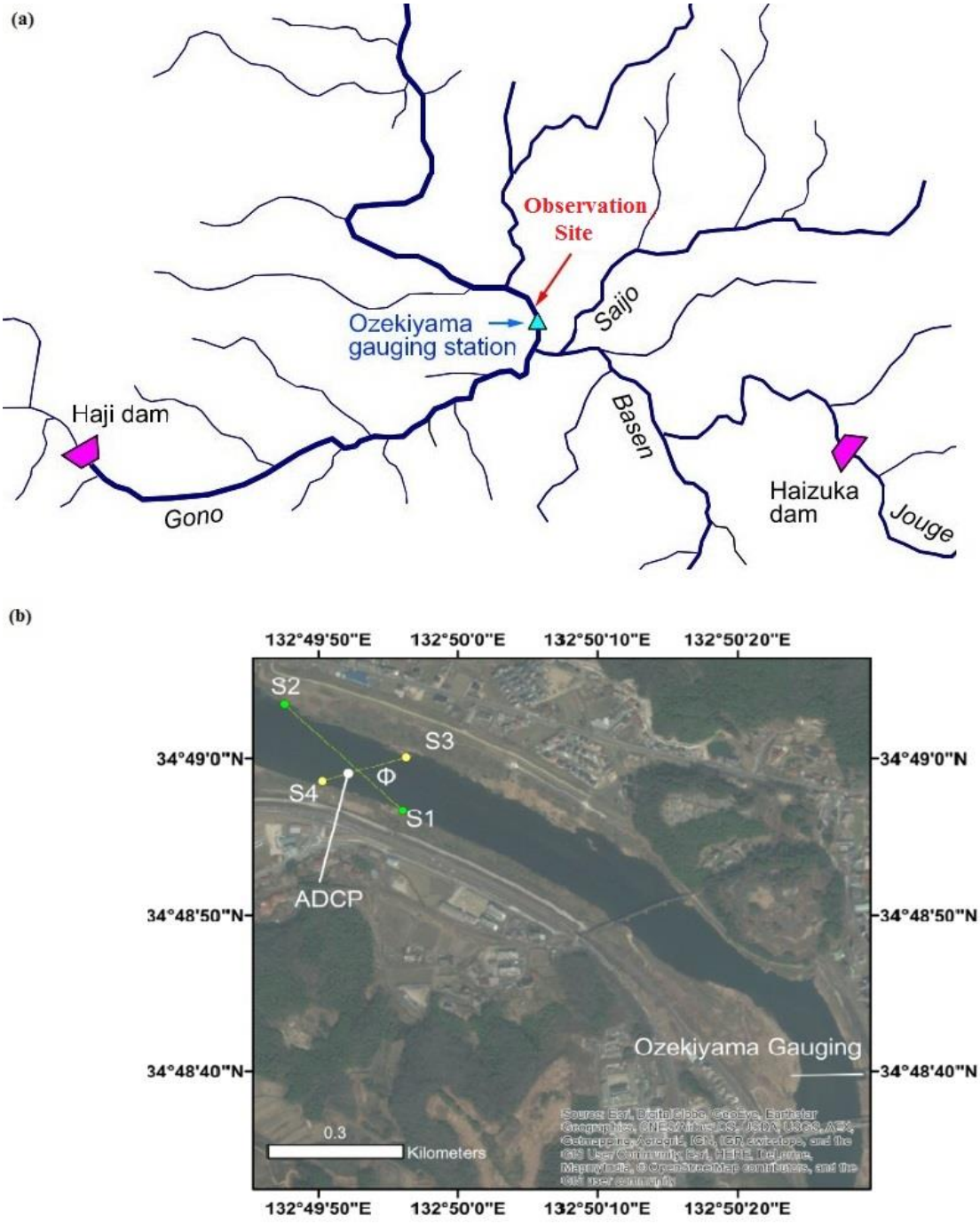

Figure 4-1 (a): Map of the river network and observation site; (b): the locations of FATS stations and ADCP.

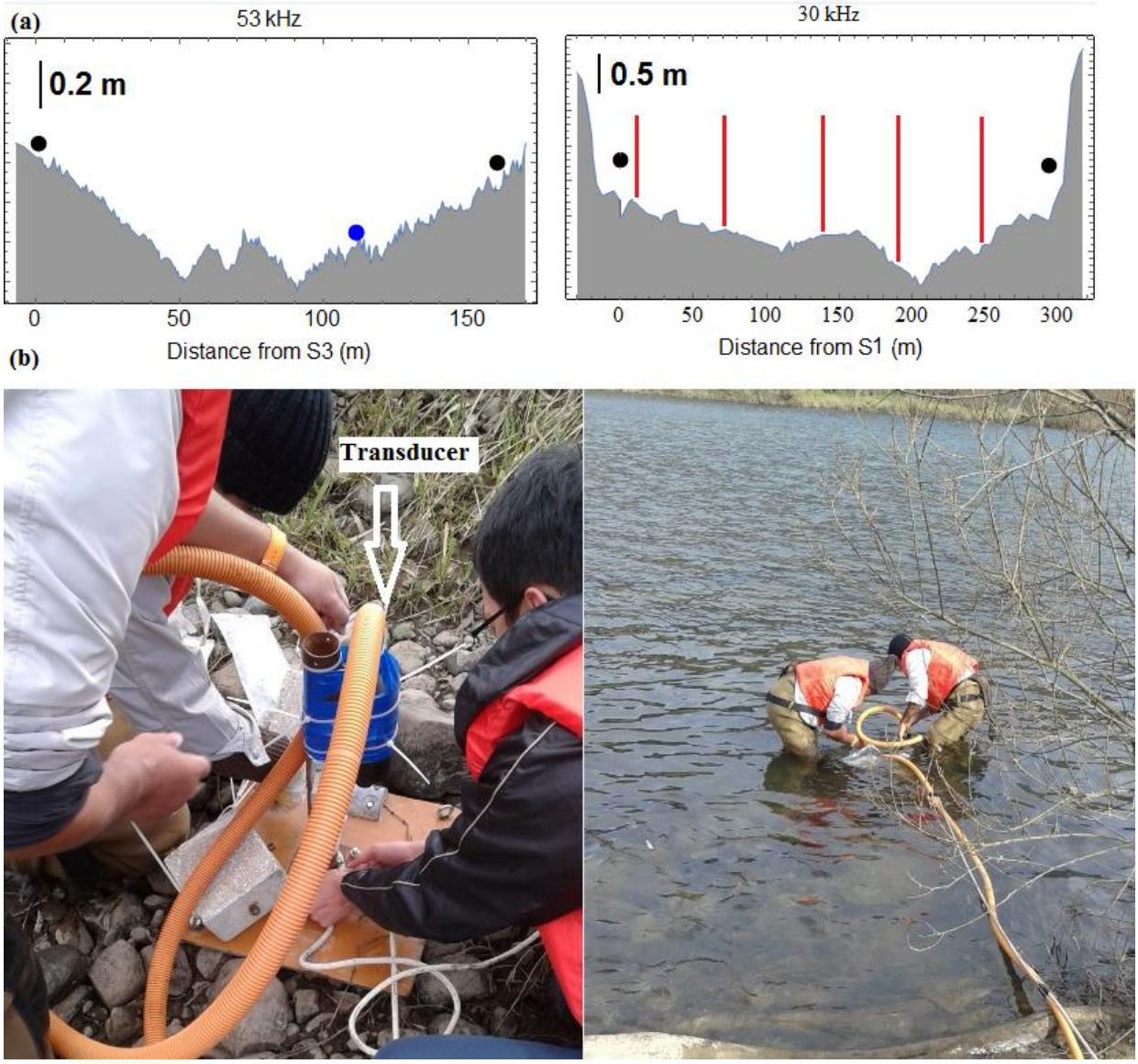

Figure 4-2 (a) Bathymetry along the 53-kHz and 30-kHz transmission paths (black points denote the transducer positions, the blue point refers to the deployed ADCP and the red lines show the positions of CTD measurement), (b) transducer installation method near the riverbank.

4.2 Data collection and processing method

In this study the FATS uses a broadband transducer (Neptune T227) with central frequency of 30 kHz and source level of 197 dB re 1 μPa at 1m at S1 and S2 stations. As well, another FAT system uses a broadband transducer (Neptune T216) with central frequency of 53 kHz and source level of 202 dB re 1 μPa at 1m at S3 and S4 stations. A ninth order M-sequence was applied to increase the processing gain by about 22.6 dB. Three cycles per digit (Q-value) was also selected as a suitable value to transmit the phase-modulated sound from the broadband transducers. T_r was three-times the period of the carrier (0.1 ms) and T_p was 102.3 ms.

The minimum distance between the two stations of FATS (L_{min}) depends on the product of the length of the sound pulse and sound speed (C), which is expressed in Eq. (4.1). In addition, the velocity resolution (u_r) is an important factor that is inversely related to the distance between the two stations and the frequency (Eq. (4.2)) [45]. Therefore, the velocity resolution has the lowest value at the minimum length between the stations:

$$L_{min} = \frac{Q\text{-}value}{frequency} \times (M\text{-}sequence\ digits) \times C \tag{4.1}$$

where the ninth order *M-sequence digits* is 511. Q-value was set to 3.

The velocity resolution is given by:

$$u_r = \frac{{c_m}^2}{2L}\frac{1}{2f} \tag{4.2}$$

As previously mentioned, the determination of the flow angle (θ) requires extra devices such as a moving-boat ADCP [50]. In this study, a new equation is proposed to estimate the flow direction using two crossed acoustic transmission lines.

Based on the condition of continuity, the streamflow in both sections of S1–S2 and S3–S4 should be equal (Figure 4-1); thus, θ is derived as follows:

$$Q_{1\text{-}2} = Q_{3\text{-}4} \tag{4.3}$$

Hence:

$$A_1(H_1) \times u_1 \tan\theta_1 = A_2(H_2) \times u_2 \tan\theta_2 \tag{4.4}$$

where A is the cross-sectional area along the sound path and is a function of the water level H, θ_1 refers to the angle between the S1–S2 line and the stream flow direction and θ_2 denotes the angle between the S3–S4 line and the stream flow direction.

According to Figure 4-1, $\emptyset$ is the angle between the two cross paths; substituting the value of $\theta_2 = \emptyset - \theta_1$ in Eq. (4.4) gives the following equation:

$$\theta_1 = \tan^{-1}\left[\frac{u_2 A_2}{u_1 A_1}\ \tan(\emptyset - \theta_1)\right] \tag{4.5}$$

As a result, θ_1 is obtained by Eq. (4.5) but it requires an iterative method. Using trigonometric expansion, Eq.(4.5) is changed to an explicit form as:

$$\theta_1 = \cos^{-1}\left(\frac{1}{2}\sqrt{\frac{\sqrt{2}\cos(\phi)\sqrt{A_1{}^2u_1^2+\cos(2\phi)\,(A_1u_1\text{-}A_2u_2)^2+6A_1A_2u_1u_2+A_2^2u_2^2}+\cos(2\phi)\,(A_2u_2\text{-}A_1u_1)+3A_1u_1+A_2u_2}{A_1u_1+A_2u_2}}\right) \tag{4.6}$$

where $\emptyset$ is the angle between two cross paths. The $\emptyset$ can be given as:

$$\emptyset = \tan^{-1}\left(\frac{X_2Y_1 - X_1Y_2}{X_1X_2 + Y_1Y_2}\right) \tag{4.7}$$

where $X_1 = \mathrm{S1}x - \mathrm{S2}x$, $X_2 = \mathrm{S3}x - \mathrm{S4}x$, $Y_1 = \mathrm{S1}y - \mathrm{S2}y$, $Y_2 = \mathrm{S3}y - \mathrm{S4}y$. The coordinates of the acoustic stations with respect to the base point (132.83° E, 34.8158° N) are presented in Table 4-1.

Table 4-1 The coordinates of acoustic stations.

Station	Eastward (m)	Northward (m)
S1	S1x = 209.792	S1y = 0
S2	S2x = 0	S2y = 206.787
S3	S3x = 199.725	S3y = 113.711
S4	S4x = 50.778	S4y = 52.141

4.2.1 Error structure in the angle measurement

The error structure of angle estimation between the ray path and the stream line includes the five terms that are presented in Eq. (4.8).

$$\delta\theta = \delta\theta_{\emptyset} + \delta\theta_{A_1} + \delta\theta_{A_2} + \delta\theta_{u1} + \delta\theta_{u_2} \tag{4.8}$$
$$= \frac{\partial\theta}{\delta\emptyset}\delta\emptyset + \frac{\partial\theta}{\partial A_1}\delta A_1 + \frac{\partial\theta}{\partial A_2}\delta A_2 + \frac{\partial\theta}{\partial u_1}\delta u_1 + \frac{\partial\theta}{\partial u_2}\delta u_2$$

The relative error is given as:

$$\frac{\delta\theta}{\theta} = \frac{\delta\theta_{\emptyset}}{\theta} + \frac{\delta\theta_{A_1}}{\theta} + \frac{\delta\theta_{A_2}}{\theta} + \frac{\delta\theta_{u_1}}{\theta} + \frac{\delta\theta_{u_2}}{\theta} \tag{4.9}$$

The first error term ($\frac{\delta\theta_{\emptyset}}{\theta}$) is uncertainty due to the angle between the two transmission lines and has the greatest impact on the error analysis. The second and third error terms ($\frac{\delta\theta_{A_1}}{\theta}, \frac{\delta\theta_{A_2}}{\theta}$) are induced by the errors in the water level measurements and imperfect bathymetric measurements by the moving-boat ADCP for the 30-kHz and 53-kHz FAT systems, respectively. The fourth and last terms ($\frac{\delta\theta_{u_1}}{\theta}, \frac{\delta\theta_{u_2}}{\theta}$) are due to the mean velocity along the transmission lines.

4.2.2 The advantages of 53-kHz FATS

FATS is operated by a Micro Embedded System called T-SH2MB. An Integrated Timer Unit (ITU) inside the T-SH2MB controls the sound wave output. A laboratory experiment was

performed to determine the maximum transmitting and receiving frequency that the ITU can organise. The length of the sound wave can be theoretically calculated in the ITU; it can also be measured practically by an oscilloscope.

The frequency increases step-by-step and the time delay between the measured values and the theoretical value is calculated. As seen in Table 4-2, the difference between the theoretical value and the transmitted value remains low until 57 kHz. However, the difference between the theoretical value and the received value sharply increases at 54 kHz. Thus, the FATS is limited by the receiving section at 54 kHz. Therefore, 53 kHz is the maximum operational frequency for the FATS.

Table 4-2 Calculation of maximum frequency operated by FATS.

Frequency (Hz)	Measured sound wave width (Transmit) (usec)	Measured sound wave width (Receive) (usec)	Theoretical sound wave width in ITU (usec)	Time delay (usec) transmit, receive
53000	57708	57710	57697	11, 13
54000	56474	61456	56469	5, 4987
55000	55251	68135	55242	9, 12893
56000	54633	72179	54628	5, 17551
57000	55637	71246	53400	2237, 17846

According to Eq. (4.1), the minimum length between the two 30-kHz FATS stations is approximately 76 m, whereas the 53-kHz FATS can operate at distances as short as 43 m. Therefore, one of the restrictions of the 30-kHz FATS is the lack of usability in small rivers where

the 53-kHz FATS can operate. However, using both types of FATS at their minimum distances provides the lowest values of velocity resolution. Table 4-3 shows the comparison between both systems. According to Eq. (4.2), in this study, the velocity resolution for the minimum distances ranged from 0.227 m/s to 0.235 m/s due to the sound speed variations for both the 30-kHz and 53-kHz FAT systems. The sound speed varied from 1440 m/s to 1465 m/s. The velocity resolution increases with increment the distance between stations. In this study, the distances were set at 294.629 m and 161.167 m for the 30-kHz and 53-kHz FAT systems, respectively. The velocity resolution ranged from 0.058 m/s to 0.06 m/s and 0.06 m/s to 0.062 m/s for the 30-kHz and 53-kHz FAT systems, respectively. These values still represented low resolution, although the velocity resolutions improved. At this step, the relatively low velocity resolution can be increased by averaging the ensemble over 20 data points. As a result, the velocity resolution was improved to $\frac{0.06}{\sqrt{20}} = 0.013\ m/s$.

Table 4-3 Velocity resolution (u_r) depending on the frequencies and acoustic path length.

Frequency	30 kHz		53 kHz	
Acoustic path length	76 m	294.629 m	43 m	161.167 m
Velocity resolution	0.227-0.235 m/s	0.058-0.06 m/s	0.227-0.235 m/s	0.06-0.62 m/s

4.3 Arrival time of acoustic signals

4.3.1 Arrival time of 53-kHz FATS

The travel time variations of the 53-kHz data and water temperature variations, which measured by the temperature sensors attached to the transducers, are shown in Figure 4-3. The red and blue colours denote the travel times at Stations 3 and 4, whereas the black colour indicates the water temperature. As shown in Figure 4-3, the travel times of the upstream and downstream stations vary from 109.8 to 111.5 ms. From the beginning of the observation period until the middle of January 18th, the difference between arrival times at Stations 3 and 4 was 0.03 ms; this can be justified by the short distance between the transducers and the low flow-velocity. However, on the 18th, rainfall began and the flow velocity increased. As a result, greater differences in arrival times at the upstream and downstream stations reached 0.1 ms. These results show the significant influence of flow velocity on the reciprocal transmission signals.

The diurnal fluctuations of travel times between January 14th and 19th correspond to the water temperature variations, which significantly affected the sound speed. As a result, the travel times at both stations decreased during the day and increased at night. From the onset of rainfall to the end of the experiment date, the water temperature declined by around 3°C, which caused the increment in travel times.

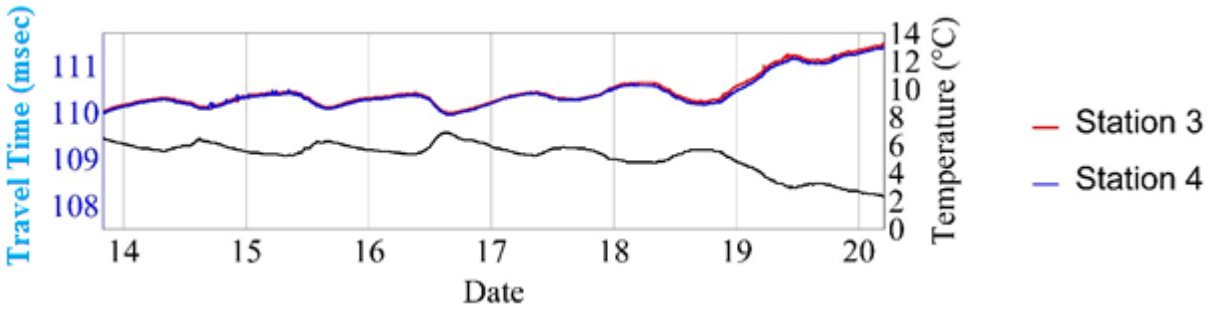

Figure 4-3 Arrival time of 53-kHz system.

4.3.2 Arrival time of 30-kHz FATS

An analysis of the 30-kHz FATS data showed that two series of travel times were detected at each station. It was observed that 28% of the recorded signals arrived in the first group and 72% of the recorded signals arrived in the second group, which had a delay of approximately 0.4 ms. This trend was almost constant throughout the experiment, even during high-flow conditions. All signal travel times are shown in Figure 4-4; the travel times of the upstream and downstream stations ranged from 205.2 to 208.6 ms. In contrast to the 161-m length of section S3–S4, the length of section S1–S2 is 296.6 m. Therefore, the difference between travel times at Stations 1 and 2 is greater than that of the 53-kHz FATS and varies from 0.2 ms to 0.4 ms.

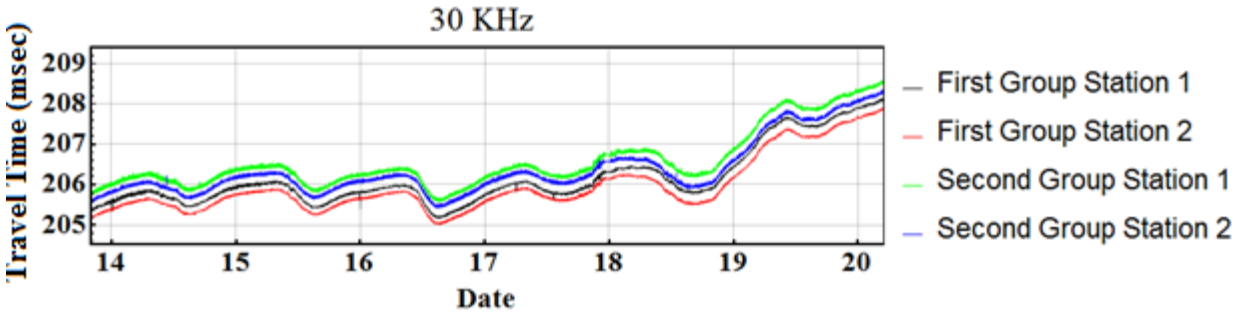

Figure 4-4 Arrival time of 30-kHz system.

4.4 Influence of bottom topography on sound wave propagation (Ray tracing)

The acoustic propagation models fall into four major classes: ray theory, spectral integration, normal mode and the PE models [84]. In this study, to verify the existence of two ray paths through the 30-kHz transmission line, a numerical simulation of sound propagation was performed using the ray theory method. Vertical sound speed profiles were measured using a Sontek Cast-Away CTD at five positions along the 30-kHz transmission line (Figure 4-2 (a)) and were used to simulate the ray pattern.

The ray simulation was implemented by solving the following differential equation:

$$\frac{d\varphi}{dr} = \frac{\partial c}{\partial r}\frac{1}{c}\tan\varphi - \frac{\partial c}{\partial z}\frac{1}{c} \tag{4.10}$$

$$\frac{dz}{dr} = \tan\varphi$$

$$\frac{dt}{dr} = \frac{\sec\varphi}{c}$$

where φ is the angle of the ray measured from the horizontal axis *r, z* is the vertical coordinate and *t* is the travel time.

Many factors, including the existence of internal waves, temperature gradients and reflection from the bottom and water surface, can affect the travel times of acoustic signals in the ocean. As a result, multipath signals with different arrival times can be observed [85]. In shallow estuaries, saline wedge intrusions generate strong haloclines and transverse density gradients and cause multipath acoustic signals to have different arrival times [48]. However, in shallow freshwater rivers, only the riverbed shape mainly affects the propagated acoustic signals because the temperature profile was insignificant and the salinity is zero.

In this study, the variations of sound speed along the transmission line were less than 1 m/s and did not have a significant effect on the acoustic ray pattern (Figure 4-5). The results of the ray simulation showed two main groups of acoustic signals with different travel times. As shown in Figure 4-5, the second group of the transmitted signal passed the entire cross section. 200 m from the left side, the riverbed has a distinctive shape that is not covered by some part of the transmitted signal. Thus, the first group of the sound does not pass through the entire cross section.

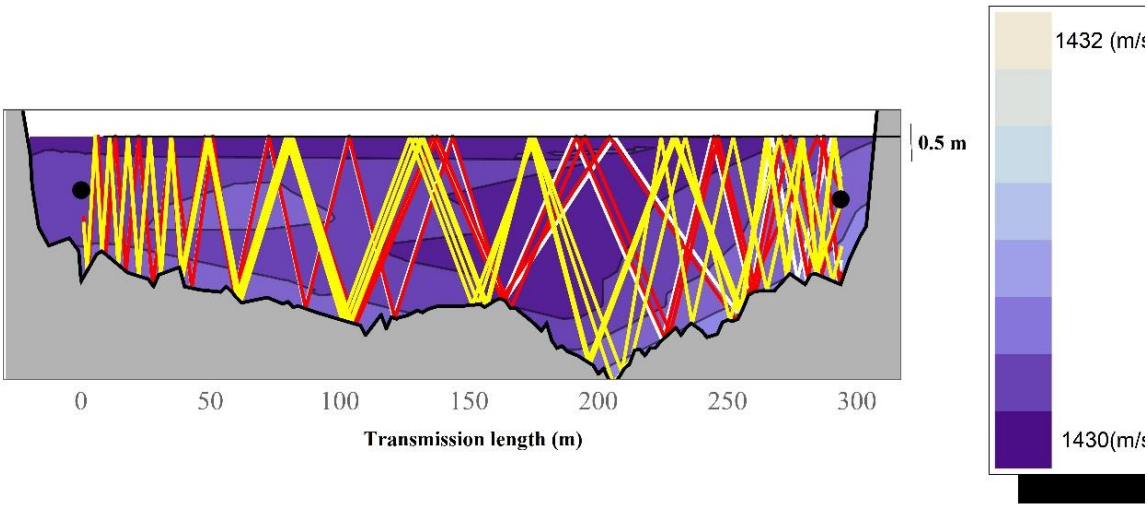

Figure 4-5 Ray simulated pattern (black disks denote to the 30-kHz transducers; red and yellow colours show the first and second groups, respectively).

In previous studies, the bed was flatter along the 30-kHz transmission line and only one group of acoustic signals was observed [18]. After that experiment, a heavy rainstorm occurred on July 23rd 2016, which raised the river discharge to 1200 m^3/s that the two groups are keeped. The flood eroded the bed near Station 2, where a local constriction existed (Figure 4-2 (b)). Thus, the eroded bed in this area is the reason for the presence of two acoustic groups.

Apart from mapping the ray pattern, another advantage of ray simulation is arrival time estimation, which allows for signal arrival times to be calculated theoretically. The results shown in Figure 4-6 also show two main groups arriving at 205.5 ms and 205.9 ms, the difference lag is 0.4 ms. This result reveals the results shown in Figure 4-4.

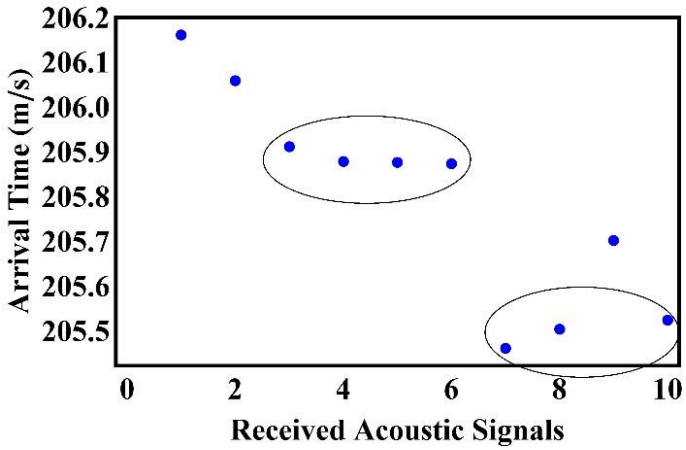

Figure 4-6 The simulated arrival times using the ray tracing technique.

4.5 Determination of flow direction

The variations of the cross-sectional area of both systems are illustrated in Figure 4-7 (a). Because the transmission line of the 30-kHz system is longer than that of the 53-kHz system, its cross-sectional area is much larger. The recorded arrival times of the acoustic signals employed in Eq. (2.12) and the mean velocity along the transmission lines were calculated. The mean velocity estimated by the 53-kHz system, varies from 0.2 m/s to 0.4 m/s. However, some anomalies are observed during the experiment, as shown by the arrows in Figure 4-7 (b). The error bars 95% confidence interval of 53-kHz FATS are less than 0.05 m/s.

As the 30-kHz system had two arrival time series, the velocity results of the first and second groups are shown in Figure 4-7 (b) in red and blue, respectively. The difference in velocity between the two groups was less than 0.01 m/s. In the present study, the 72% data that passed the entire cross section was used to estimate the mean velocity for the 30-kHz system. The measured mean velocity

along the 30-kHz transmission line varies from 0.6 m/s to more than 1 m/s. the error bars of 30-kHz FATS are 0.1 m/s.

The significant velocity difference between the 53-kHz and 30-kHz systems is due to the inclination of the transmission lines with respect to the flow direction. In other words, the angle between S1–S2 and the flow direction (θ_1) was less than the angle between S3–S4 and the flow direction (θ_2); thus, the velocity along the transmission line of the 30-kHz FATS is always greater than the measured velocity along the transmission line of the 53-kHz FATS.

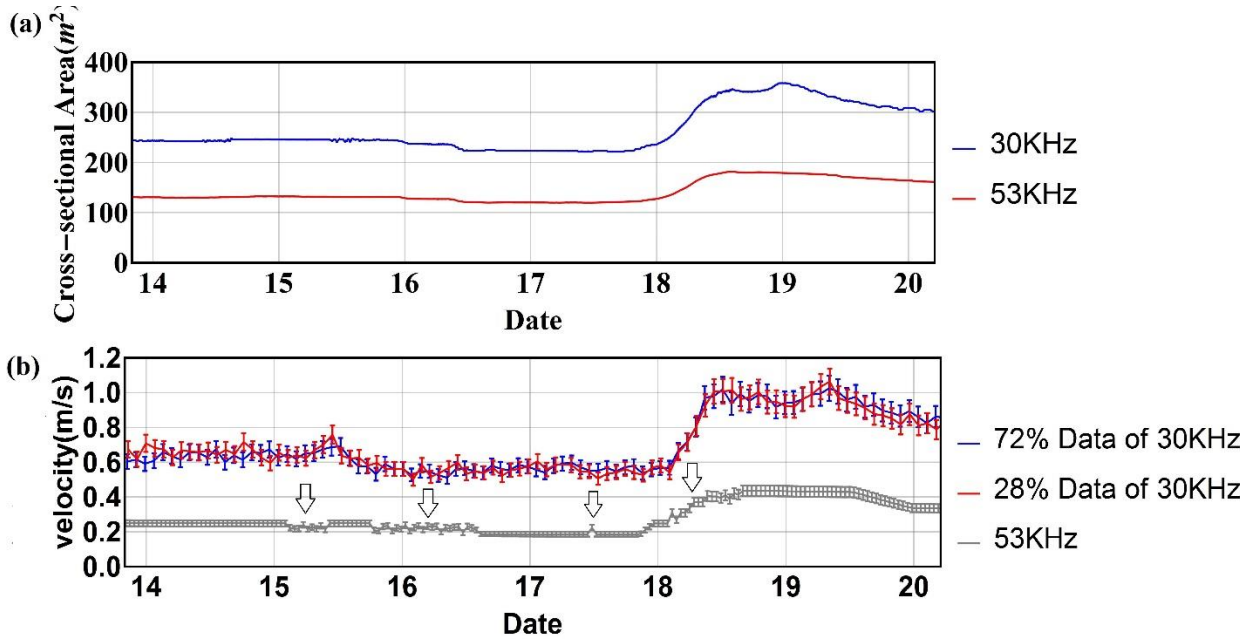

Figure 4-7 (a) Variations of water area and (b) mean velocity along the transmission lines (arrows denote anomalies in the system) with the error bars.

The cross-sectional area and the measured velocities of the 53-kHz and 30-kHz systems were substituted into Eq. (4.6) to estimate the streamflow angle between the flow direction and the

transmission lines of FATS. The results of the proposed method were compared to those of the up-looking ADCP (Figure 4-8 (a)).

As for the anomalies in the 53-kHz FAST, an overestimation of angle measurement was observed several times and are denoted by the arrows in Figure 4-8 (a); the variations of the ADCP measurements fit the FATS results during the entire period. The angle θ_1, as measured by ADCP, varied between 12 and 18°, with an averaged value of 15.2°; the estimation of averaged θ_1 gained from FATS was 15.02°. Using a 10-hour moving average, the R^2 between the two methods was 0.78 (Figure 4-8 (b)). This low R^2 was due to differences in the periods highlighted in Figure 4-8 (a) and (b). It can be concluded that the proposed method provides acceptable efficiency for estimating the angle between the flow direction and the FATS transmission line.

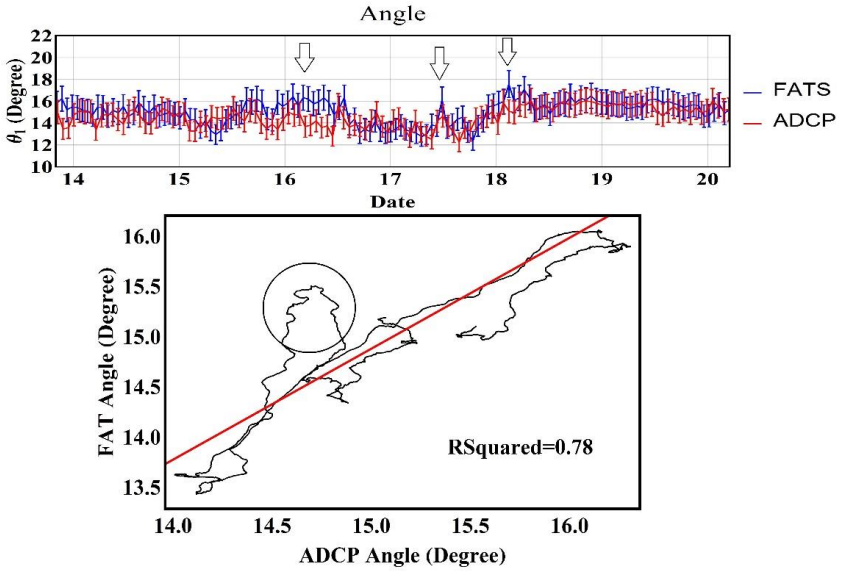

Figure 4-8 (a): Variations of θ_1 with the error bars and (b): the correlation of ADCP and FATS measurements.

4.6 Discharge calculation

Streamflow is usually estimated indirectly by the RC method [19]. The estimated discharges from the 53-kHz and 30-kHz FATS were compared to the discharge obtained by the RC method. Moreover, four transections of moving-boat ADCP were performed to validate the FATS measurements [20] (Figure 4-9 (a)). The moving-boat ADCP measurements were post-processed with WinRiver II software (Teledyne RD Instruments). The ADCP does not measure the areas at the surface and near the bottom of river [21, 22]. Furthermore, the ADCP cannot measure the discharge at the channel edges where the water is very shallow. The WinRiver II software extrapolates and estimates the discharge in these regions. In this experiment, in the all ensembles the portion of bad bins did not exceed 1% and bad ensembles in each transect were not more than 3%. Hence, the maximum error of the ADCP measurement did not exceed 5% [20].

The mean discharge until January 18th was 40 m^3/s; and then increased to 95 m^3/s due to the rain. The relative differences between the streamflow measurements of the 30-kHz and 53-kHz with RC methods are shown in blue and red colours, respectively. The relative errors of both systems are less than 10%, which are deemed acceptable error rates (Figure 4-9 (b)).

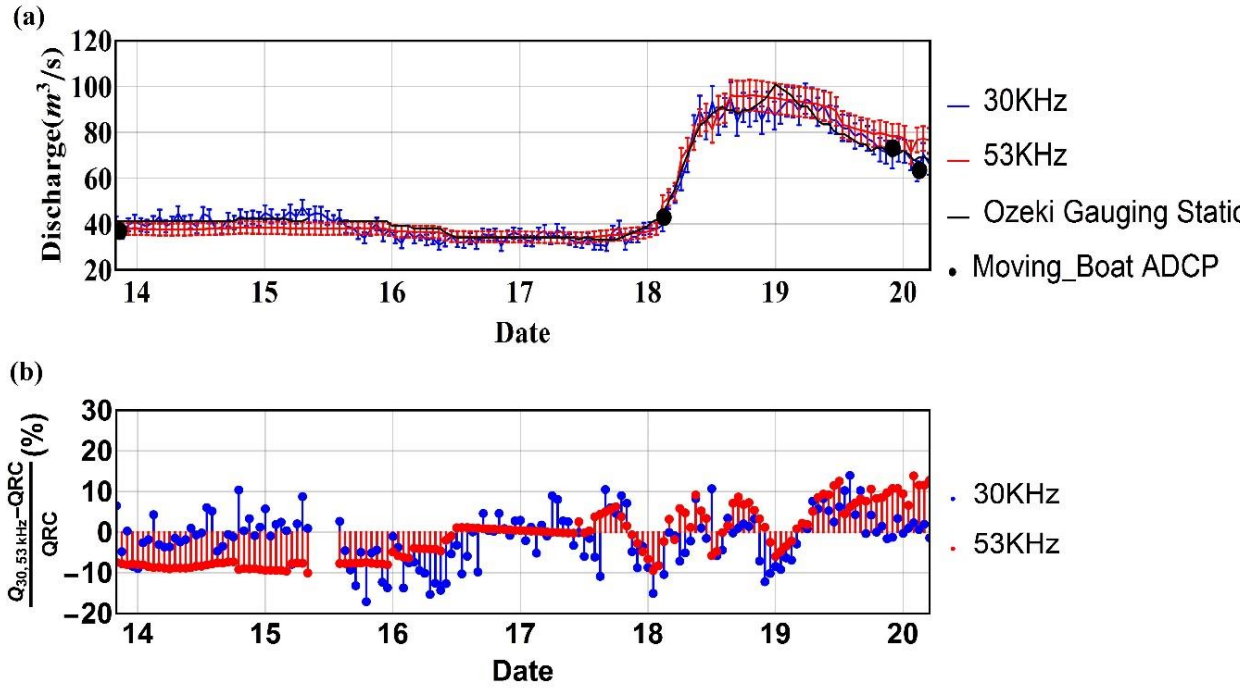

Figure 4-9 (a): Discharge measurement with the error bars and (b): relative error of FATS.

Although the FATS measure the river discharge continuously, there would be some limitations of using this system. As an example, during flood events, some floating objects such as weeds or tree branches can attach to the transducers and hinder receiving signals [14]. Additionally, the presence of large amount of suspended sediment in the flow can attenuate acoustic signals [23].

It seems that these limits are more significant for other acoustic instruments, such as AVM, ultrasonic velocity meter (UVM) and horizontal acoustic Doppler current profiler (H-ADCP) that measure streamflow continuously [24-26]. Falvey [27] showed that the refractions of the acoustic path under stratified conditions cause unacceptable uncertainties in determination of the flow rate in the AVM measurement. Furthermore, the attenuated acoustical signal in flood events or turbid

waters leads to inadequate results in the H-ADCP measurement because the horizontal profile range of H-ADCP rapidly decreases with an increase in the SSC. Moreover, in shallow streams, the main and side lobe beam interference contaminates the data because of surface or bottom reflection [14].

4.7 Error analysis results of angle estimation

As shown in Eq. (4.9), the relative error ($\frac{\delta\theta}{\theta}$) of the angle estimation between the ray path and the stream line is a function of the angle between two transmission lines ($\emptyset$), the cross-sectional area (A) and the velocity along the transmission line (u). The effect of each term is formulated and presented in Appendix 1. According to the equations that are presented in Appendix 1, the effects of the A and u are insignificant and can be ignored; however, the error in $\emptyset$ determination may cause major error in the angle estimation between the ray path and the stream line (θ).

Figure 4-10 shows the angle error variations ($\frac{\delta\theta}{\theta}$) associated with the uncertainty of $\emptyset$. In this study, the $\emptyset$ is obtained from the positions of stations measured by a GPS receiver (Wintec WBT-201/G-Rays 2). The maximum error of this brand of GPS receiver is 2 m. In this study, the angle between two transmission lines ($\emptyset$) was 67° and its error was $|\delta\phi| = 1.2°$. Hence, the relative error induced by the uncertainty in the angle measurement between the two transmission lines $\left|\frac{\delta\theta_{\emptyset}}{\theta}\right|$ is approximately 0.51 %, which is considered to be acceptable (Figure 4-10).

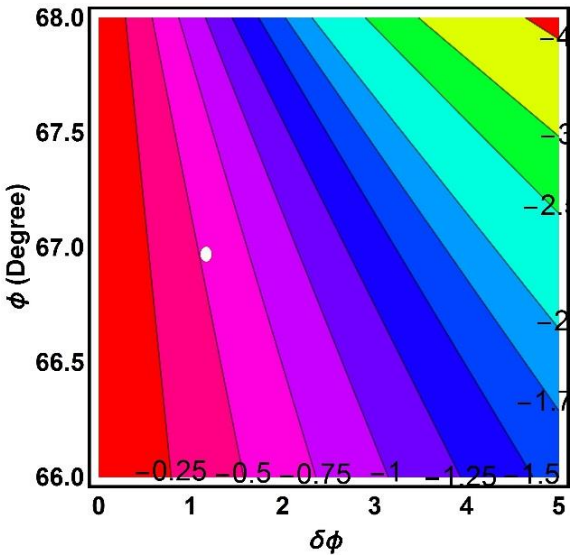

Figure 4-10 Relative error (%) of angle estimation between ray path and the stream line (θ) due to the error of the angle between two transmission lines.

4.8 Error analysis results of discharge measurement

The uncertainty associated with river discharge measurements using the both FATs is estimated by Eq. (2.18). The first and second error terms ($\left|\frac{\delta Q_{h_m}}{Q}\right|, \left|\frac{\delta Q_{A_B}}{Q}\right|$) are the function of mean water depth and the mean bed level, that need an accurate bathymetric survey to minimize these error terms. In this study, the river bathymetry was measured by the moving-boat ADCP. The uncertainty of ADCP measurement was 0.05 m [20]. Thus, the first error term for 53-kHz FATS was $\left|\frac{\delta Q_{h_m}}{Q}\right| = 0.5 - 1.6\%$, as the range of the water depths (0.6-1 m). Likewise, the uncertainty for 30-kHz FATS was $\left|\frac{\delta Q_{h_m}}{Q}\right| = 0.7 - 1.8\%$, as the range of the water depths of 0.4 m and 0.8 m. Consequently, the second error term that is the related to the cross-sectional area over the water depth, varied from 1.6 to 3.7% and 2.8 to 4.3% for 53-kHz FATS and 30-kHz FATS, respectively.

As a result, in the extremely shallow streams or during low-flow conditions, the error due to the cross-sectional area would be significant.

The third error term $\left|\frac{\delta Q_{u_m}}{Q}\right|$ depends on the velocity resolution of FATS. The velocity along the transmission lines ranged from 0.2 m/s to 0.45 m/s for 53-kHz and 0.6 to 1.05 m/s for 30-kHz FATS (Figure 8 (b)). Hence, the uncertainty due to the velocity resolution for 53-kHz FATS was $\left|\frac{\delta Q_{u_m}}{Q}\right| = 1.6 - 4.3\%$ and for 30-kHz FATS was $\left|\frac{\delta Q_{u_m}}{Q}\right| = 1.3 - 2.6\%$.

The last term of discharge uncertainty $\left|\frac{\delta Q_{\theta}}{Q}\right|$ is due to the angle between the ray path and the stream line. In this study, the uncertainty due to the angle between the ray path and the stream line was $\left|\frac{\delta Q_{\theta}}{Q}\right| = 3.5\%$ and $\left|\frac{\delta Q_{\theta}}{Q}\right| = 6.8\%$ for 53-kHz and 30-kHz, respectively. Thus, the largest possible error for 53-kHz and 30-kHz FATS may be evaluated as 13.1% and 15.5%, respectively (Table 4-4).

Table 4-4 The error comparison between 53-kHz and 30-kHz FATS.

Error Term	S3-S4 experiment	S1-S2 experiment
$\left\|\frac{\delta Q_{h_m}}{Q}\right\|$%	0.5-1.6%	0.7-1.8%
$\left\|\frac{\delta Q_{A_B}}{Q}\right\|$%	1.6-3.7%	2.8-4.3%
$\left\|\frac{\delta Q_{u_m}}{Q}\right\|$%	1.6−4.3%	1.3−2.6%
$\left\|\frac{\delta Q_{\theta}}{Q}\right\|$%	3.5%	6.8%
Total Error%	7.2-13.1%	11.6-15.5%

4.9 Conclusion

We present the first observations of river discharge using the higher frequency 53-kHz FATS. The comparison between the 53-kHz FATS and the previous 30-kHz FATS shows that the minimum operational distance would be reduced from 76 m to 43 m using the 53-kHz FAT system. Moreover, the velocity resolution approximately doubles when using the 53-kHz FAT system. The validation of discharge estimation was done by ADCP measurements and RC method for 40–100 m^3/s. The relative errors were less than 10% and therefore confirm the reliability of FATS measurements. This study also showed that in contrast to the estuaries where the salinity intrusion causes the existence of different acoustic signals, in the freshwater rivers, the riverbed topography is the reason for the existence of different acoustic arrival times. The results of uncertainty analysis showed that the error term due to the FATS velocity resolution ($\left|\frac{\delta Q_{u_m}}{Q}\right|$) depends on the system

frequency and the distance between the transducers. Hence, a higher frequency of FATS would reduce this error factor. Inaccurate determination of the angle between flow direction and the transmission line of FATS, may cause large error in discharge measurement. Hence, a new equation was proposed to determine the angle accurately and minimise this error factor. It was observed that the uncertainty of angle determination was 0.51%. The measured angle varied from 12 to 18° and the result of the angle comparison with the ADCP deployed near the intersection of acoustic paths shows the efficiency of the proposed method.

5. Application of FATS to Ota Estuary

Estuaries are complex coastal environments due to physical factors such as tidal currents, river flow, sediment transportation, waves and wind [86]. Namely, tides and tidal currents are a great source of energy, contributing to turbulence and mixing in these coastal environments [87]. Hence, unlike the freshwater rivers, the flow structure in estuaries is complex because the hydrodynamics of such environments is controlled by a combination of multiple processes, including salt intrusion, tidal process and freshwater discharge. Thus, understanding the flow characteristics in estuaries, especially when the balance between river discharges and marine processes is reversing, is important for researchers.

Better understanding of how currents vary in estuaries requires continuous monitoring of flow by different instruments, such as ADCPs. Bottom-mounted ADCPs measure the vertical profile of flow velocity at a fixed point in a river. This method cannot estimate cross-sectional mean velocity. The moving-boat ADCP combined with accurate navigation (such as GPS) can measure the velocity in rivers and estuaries [26,120,121]. However, the spatial variation of the tidal currents in the estuaries is fast and moving-boat ADCP may be not able to measure the streamflow continuously; moreover, calculating the residual currents and removing the tidal currents would be difficult and involves complex methods [122-126]. Hence, new instruments that are able to measure mean flow velocity and residual currents continuously are be needed. FATS can fill this role in addition to efficiently measuring flow characteristics in freshwater rivers. Unlike the

moving-boat ADCP, FATS can easily measure the speed of tidal currents continuously and can calculate the residual currents without complex steps.

5.1 Experiment site and deployment

A 10-km reach of the Ota Estuary, located in Hiroshima City, was selected as the study site (Figure 5-1). The Ota Estuary bifurcates into two main branches about 9 km upstream from the mouth: the Old Ota River and the Ota Diversion Channel. Like many estuaries, this estuary is regulated by upstream floodgates. The Oshiba Floodgate, located in the Old Ota River, consists of a movable weir with three gates and a fixed weir, which is always completely open. The Gion Floodgate, which is located in the Ota Diversion Channel, consists of three movable sluice gates, of which only one is usually open. The freshwater discharge before bifurcation can be estimated using RCs at the Yaguchi Station, which is located 14 km upstream from the mouth and is not tidally modulated. The upstream border of the tidal compartment is located about 13 km upstream from the mouth. The water level fluctuations are measured at the mouth of the Ota Diversion Channel (Kusatsu Station) and near the bifurcation of the Ota River at Gion Station. The tides are primarily semi-diurnal but mixed with a diurnal component. The tidal range at the mouth (Kusatsu Station) varies in a range from 0.3 m to 4 m. One of the branches of Ota Estuary, called the “Kyu Ota River”, was selected to carry out the velocity measurement observations by FATS.

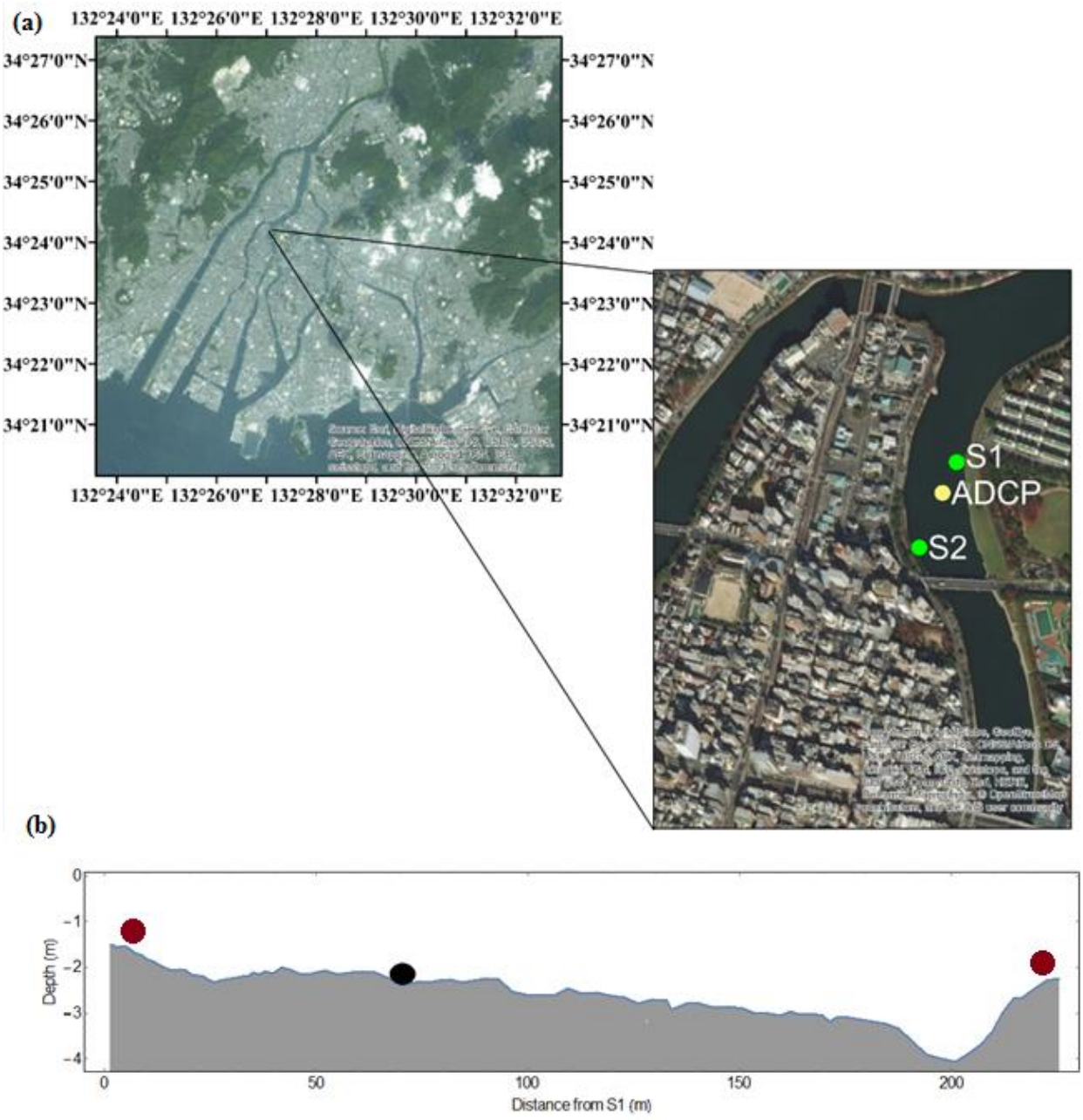

Figure 5-1 (a) Study area and experimental site and (b) oblique cross section of river and the position of the two FATS stations and the ADCP.

Measurement of flow velocity was performed by FATS during a 48-hour period from June 7th to 9th, 2016. The FATS was equipped with two 30-kHz broadband transducers with horizontally omnidirectional and vertically hemispherical beam patterns. The horizontal distance between two stations was about 215 m. The acoustic pulses were triggered by a GPS clock and were transmitted simultaneously from both transducers every 30 s.

An upward looking 2MHz-ADCP was also deployed near the middle of transmission line of FATS to measure the flow velocity. The pulse interval was set to the 600 s with the 0.1m cell size. The blanking distance was 0.1 m. The ADCP provided velocity data, tidal level record and current direction.

Table 5-1 ADCP settings.

Parameter	Value
Profile interval (s)	600
Cell size (m)	0.1
Average interval (s)	300
Blanking distance (m)	0.1

5.2 Data collection and processing method

Numerical model

The shallow-water equations (a depth-integrated form of the Navier–Stokes equations) consist of three equations. An equation for conservation of mass that is presented by Eq. (5.1) and two other equations for the conservation of momentum in the horizontal directions: Eqs. (5.2) and (5.3) [92].

$$\frac{\partial h}{\partial t}+\frac{\partial}{\partial x}(hu)+\frac{\partial}{\partial y}(hv)=0 \tag{5.1}$$

$$\frac{\partial u}{\partial t}+u\frac{\partial u}{\partial x}+v\frac{\partial u}{\partial y}+g\left(\frac{\partial h}{\partial x}+\frac{\partial z_0}{\partial x}\right)-\frac{\epsilon_{xx}}{\rho}\frac{\partial^2 u}{\partial x^2}-\frac{\epsilon_{xy}}{\rho}\frac{\partial^2 u}{\partial y^2}+\frac{gu}{C^2 h}\sqrt{u^2+v^2} = F_x \tag{5.2}$$

$$\frac{\partial v}{\partial t}+u\frac{\partial v}{\partial x}+v\frac{\partial v}{\partial y}+g\left(\frac{\partial h}{\partial y}+\frac{\partial z_0}{\partial y}\right)-\frac{\epsilon_{yx}}{\rho}\frac{\partial^2 v}{\partial x^2}-\frac{\epsilon_{yy}}{\rho}\frac{\partial^2 v}{\partial y^2}+\frac{gv}{C^2 h}\sqrt{u^2+v^2} = F_y \tag{5.3}$$

where x and y are the Cartesian coordinates in a horizontal plane; u and v represent the depth averaged velocity in the x- and y-directions; t time; h the water depth; ϵ_{xx}, ϵ_{xy}, ϵ_{yx}, and ϵ_{yy} are eddy viscosity coefficients; C is the Chezy coefficient ($=\frac{h^{1/6}}{n}$ for metric units, n = Manning's roughness coefficient); g is gravity; ρ is the fluid density; z_0 is the channel bottom elevation and F_x and F_y are optional terms incorporating Coriolis and wind forces acting in the x and y directions. These equations have been used widely by researchers [128-[94]130].

RMA2 is a famous 2-D depth-averaged finite-element hydrodynamic numerical model that uses the above equations to solve the shallow-water equations [96]. The early model of RMA2 was proposed by Norton et al. [97] and developed by King [98] to calculate water-surface elevations and horizontal velocity components in subcritical free-surface turbulent flows. RMA2 is widely used by researchers [134-138].

RMA2 uses the finite-element method and solves Eqs. (5.1)– (5.3) for u, v and h at each node within a finite-element mesh and allows velocity and depth values to be interpolated across elements such that the model's output represents a continuous field of flow velocity and water depth. The input data required to run RMA2 mainly consist of four things: bathymetry data describing the channel geometry, boundary conditions, channel-bed roughness coefficients (Chezy or Manning values) and eddy viscosity values [101]. Bathymetry data is collected in the form of XYZ coordinates. Roughness values are assigned to a particular element based on the material properties visually observed at that element's location within the study area. Similarly, one can specify eddy viscosity values that are characteristic of each bed material and assign viscosity values for each element depending on the bed material found at that element's location. The usual means of applying boundary conditions in RMA2 is to specify a total flow rate at the upstream boundary and a water surface elevation at the downstream boundary. According to USACE, 80% of the ability to produce accurate model results depends on using appropriate bathymetry data, mesh design and boundary conditions [102].

Bathymetry data and boundary conditions

Bathymetry data for the study site was collected in the form of XYZ coordinates of MLIT. Bathymetry mesh consists of 9453 elements and 25736 nodes (Figure 5-2). In this research, eight-nodded quadratic mesh and two-dimensional depth-averaged finite-element were applied. Boundary conditions for the study site were established by measuring discharge at the Yaguchi gauging station located upstream the study area and surveying tidal elevations at the Kusatsu gauging station (34°21'46.00" N, 132°24'14.00" E) located at the mouth of estuary. The model was simplified and the effects of Gion and Oshiba gates were ignored.

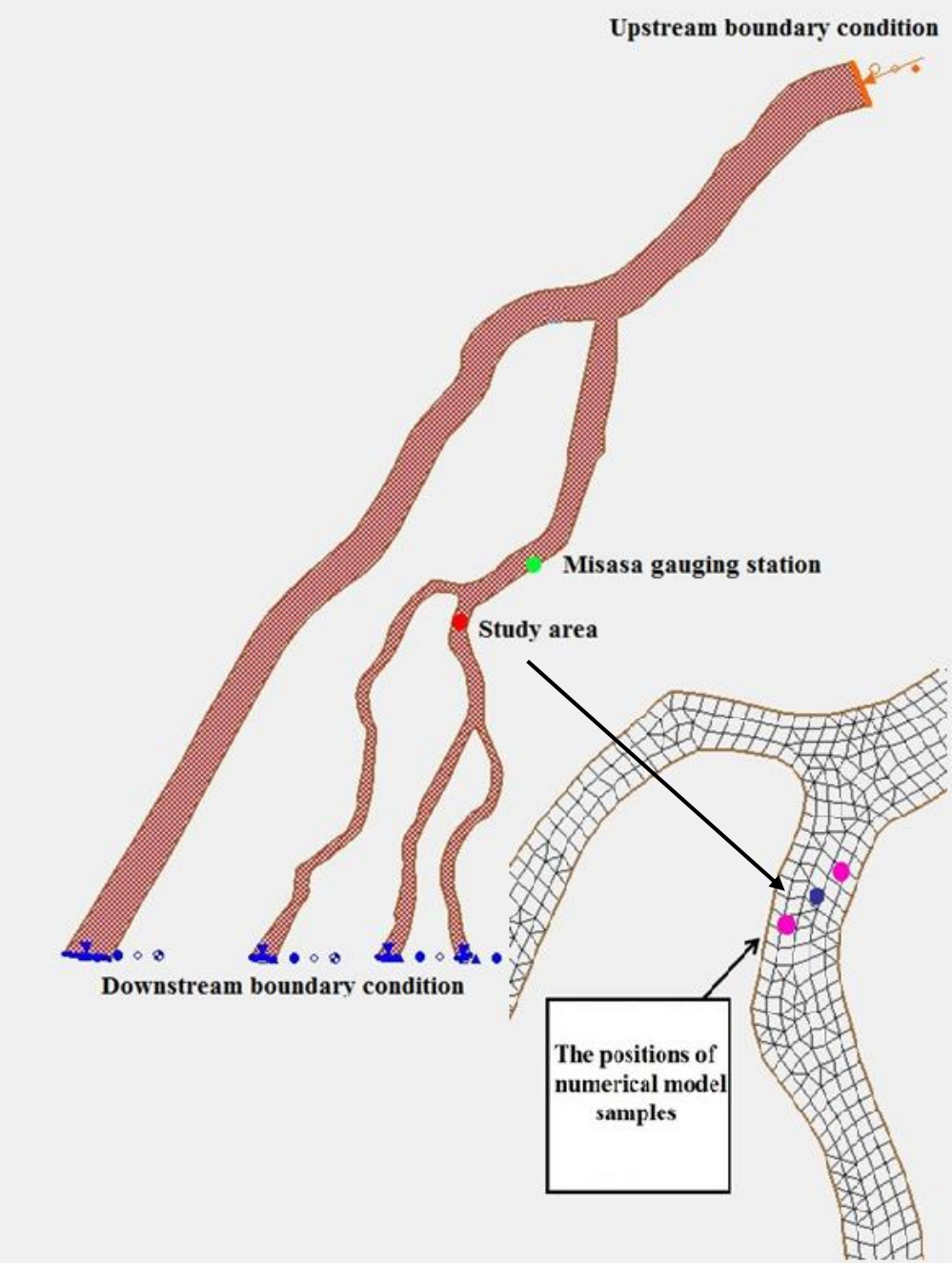

Figure 5-2 Finite-element mesh of the Ota Estuary and the location of boundary conditions and study area.

5.3 Validation of FATS velocity

The instruments captured two ebb and flood tides during the study period. The ADCP measures the velocity magnitudes in streamwise (s), transverse (t) and vertical (v) components. In this study, the streamwise component is compared to the FATS velocity measurement. As shown in Figure 5-3 (a), the comparison between FATS and ADCP shows that the FATS velocity value is larger than that of ADCP in the ebb tides, whereas it is smaller than the ADCP velocity in the flood tides. This is because the moored ADCP measured the velocity in the column of water at one point of river cross section, while FATS measured the cross-sectional averaged velocity. Hence, the ADCP is not able to represent the mean velocity of the river. In this period, the velocity varied between -0.2 m/s and 0.85 m/s in the flood and ebb tides, respectively. Hence, the relative errors are large and variy between -30% and 30% (Figure 5-3 (b)).

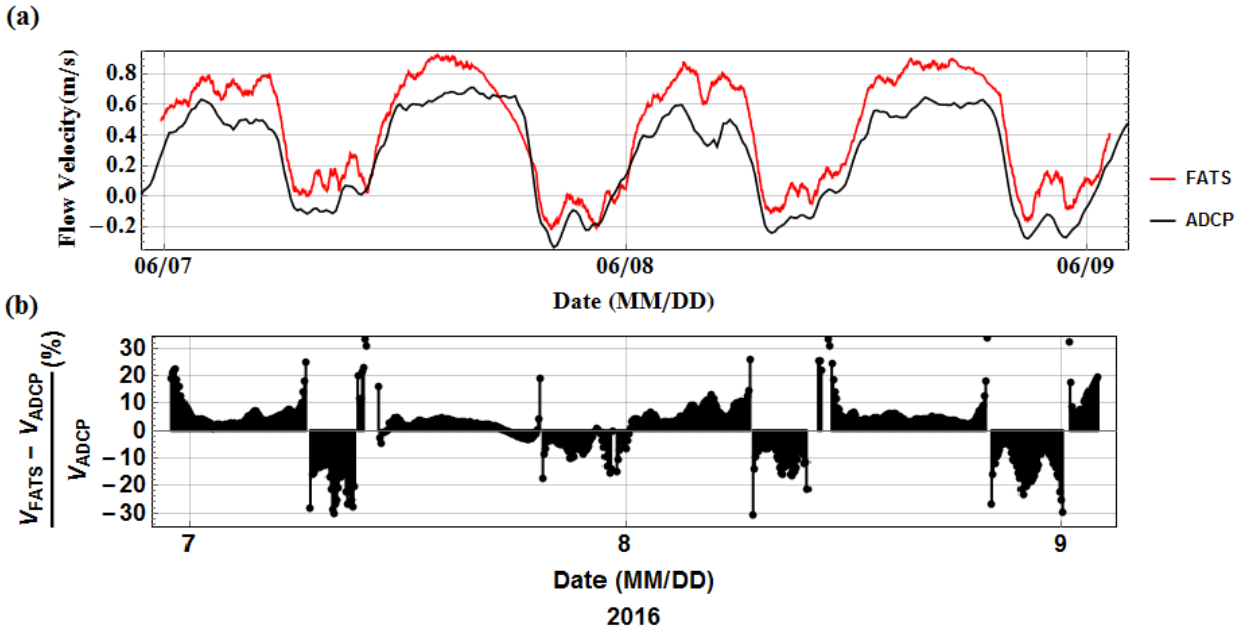

Figure 5-3 (a): The comparison of streamwise velocities measured by FATS and ADCP and (b) The relative error of velocity.

A sample position near the ADCP location (shown by the blue point in Figure 5-2) was selected to compare the numerical model results to the ADCP measurement. The numerical model presents two kinds of velocity output: scalar type and vector type. The vector velocity output was used for ADCP comparison. As shown in Figure 5-4, there is good agreement between the ADCP and the numerical model.

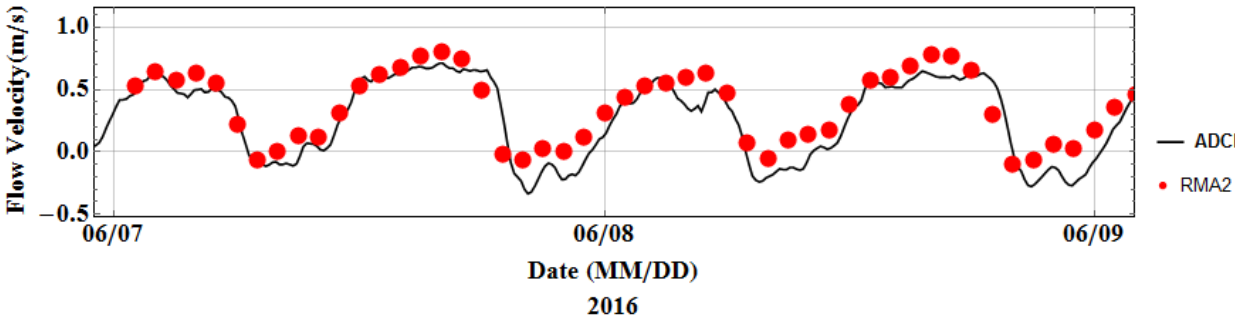

Figure 5-4 The comparison of the numerical model result and the ADCP measurement.

In the previous comparison between ADCP and the numerical model, one point of the numerical model (shown by the blue point in Figure 5-2) was chosen to compare with the ADCP result. As the FATS measures the cross-sectional average velocity, three points of the numerical model, which are located along the transmission line of FATS, were selected to compare with the FATS data (Figure 5-2). The averaged velocity of three points was calculated and compared with the FATS measurement result (Figure 5-5 (a)). As a result, the relative errors were less than 25% that shows FATS can be a useful instrument to validate or to be used as the boundary condition of the numerical models (Figure 5-5 (b)).

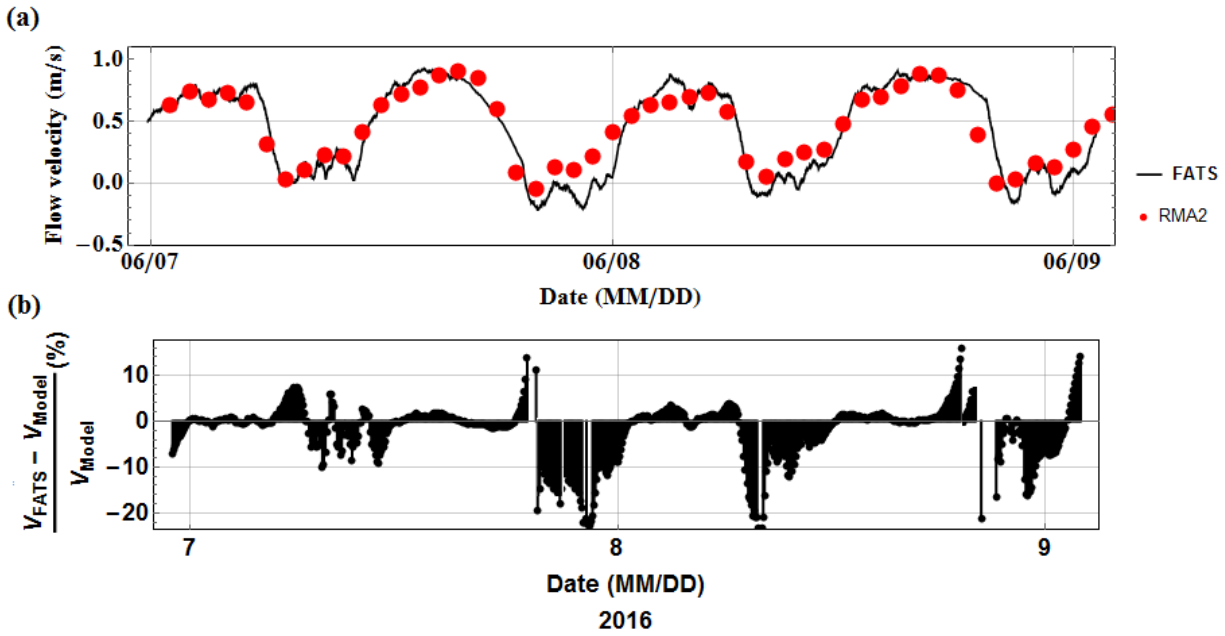

Figure 5-5. (a): The comparison of numerical model results and FATS measurements and (b): The relative error of velocity.

5.4 Conclusion

In this experiment, the river velocity and the tidal currents were measured by FATS and compared to the ADCP and the numerical result. The cross-sectional average velocity ranged from -0.2 m/s to 0.85 m/s in the landward and seaward directions, respectively. A moored ADCP was also deployed close to the centre of river, along the FATS transmission line, to measure the velocity components. The streamwise velocity was differ from the velocity data obtained by FATS because the ADCP measured a column of water at one point of the cross section and therefore does not represent the mean velocity of river. Hence, the relative error was less than 20% during the ebb tide and the relative error reached to 30% during flood tide. The numerical model was also used for comparison with the acoustic methods. The vector velocity output was used to compare with

the ADCP and FATS measurement. One point of the numerical model, located near the ADCP, was chosen to compare with the ADCP, while three points along the FATS transmission line were selected and then averaged for comparison with the FATS velocity measurements. The relative error of FATS and the model was less than 20%.

6. SUMMARY AND CONCLUSION

The main goal of this study is to continuously monitor the flow velocity, streamflow and suspended sediment concentrations in a mountainous river and tidal estuary. Worldwide, the most-often classical approach adopted in estimating the river discharge is the Rating curve (RC) method. However, the construction of ratings curves to cover the wide range of flows and processes going on in rivers has been a challenging duty due to several factors:

The RC method introduces high uncertainties in streamflow estimation, also, the application of the RC method may be impractical or not valid for complex flow conditions, such as variable backwater, tidal flow, rapid changes in flow, etc.

The main contribution of this study is to utilize the Fluvial Acoustic Tomography System (FATS) as a powerful and alternative approach for measuring the flow velocity and river discharges. In addition, to introduce new methods to minimize the uncertainties of streamflow which measured by means of FATS.

In the previous works, a 30-kHz FATS was used to measure the river discharge while a moving-boat ADCP was used to determine the angle θ. The present study successfully introduces a 53-kHz FATS that overcomes the limits of 30-kHz FATS and can be used in shorter ranges than those covered by a 30-kHz FAT system. Moreover, the flow angle is deduced by using cross-path configuration method.

In this study, three field observations were performed using the FATS. The first and second one were done in the Gono River, whereas, the last field test carried out in the Ota Estuary.

In the first field test, the river discharge and Suspended Sediment Flux (SSF) were measured by FATS. A regression analysis was applied to estimate the angle between the flow direction and the transmission line (θ). The result of θ estimation was 19.34°. The measured streamflow by FATS varied from 60 m^3/s to 270 m^3/s. The maximum SSF that was transferred in the river was 23 kg/s and the amounts of SSF due to the Haizuka and Haji dams flushing were 10 kg/s and 8 kg/s, respectively. However, the SSC comparison between FATS and OBS showed a large error in FATS estimation. It seems that the SNR of FATS is not only depends on the suspended sediment concentration, but also depends on the other factors such as water depth, bottom shape, weed accumulation, etc. Hence, further studies are needed to improve the proposed equation of <SSC> measurement.

In the second field test, we examined the higher frequency 53-kHz FATS in the Gono River and it compared with the 30-kHz FATS. Then, the flow direction fluctuations were measured by using the cross-path configuration method. The measured angle varied from 12 to 18°. The estimated angle was validated by the ADCP that confirmed the efficiency of the proposed method. Finally, the river discharge was estimated using both FAT systems and compared with the Rating Curve (RC) method. The relative errors of FATS were less than 10%. In this observation, the cross-path configuration method was proposed to determine the angle θ accurately and decrease the uncertainty due to the angle determination. As well, we applied the higher frequency FATS to improve the velocity resolution and decrease the uncertainty of discharge measurement due to the velocity component. However, the signal of 53-kHz FATS would attenuate more than that of 30-kHz FATS in turbid waters or in the wide rivers.

Last field test presented the velocity measurement by FATS in the Ota Estuary. The measured velocity was compared with the ADCP and a numerical model. The velocity ranged from -0.2 m/s to 0.85 m/s in the landward and seaward directions, respectively. It was concluded that FATS can be considered as a reliable instrument to be used as the boundary condition input of the Numerical models.

The general novel points of this study can be summarized as:

- Shows the ability of FATS to measure the suspended sediment flux.

The first attempt of SSF measurement by FATS was done in this study. The results were compared to the other instruments such as OBS and ADCP that confirmed the capability of FTAS to estimate SSF. However, the proposed equation had large error and further investigations are needed.

- Decrease the uncertainty of FATS measurement:

1- We proposed two different methods to determine the angle between flow direction and the transmission line of FATS by using either a regression analysis or a cross-configuration FATS.

2- The velocity resolution that depends on the frequency.

We applied the 53-khz FATS to increase the velocity resolution and decrease the uncertainty due to the velocity measurement.

- Shows the efficiency of FATS to validate the numerical model.

This study also shows that the FATS can be a reliable instrument to validate, calibrate or to be applied as the boundary condition of the numerical models.

Additional future investigations are suggested as:

- It is recommended to use much higher frequency of FATS to increase the velocity resolution as much as possible. However, the signal may attenuate quickly.
- It seems that the SNR of FATS is not only depends on the suspended sediment concentration, but also depends on the other factors such as water depth, bottom shape, weed accumulation, etc. Hence, further studies are needed to improve the proposed equation of <SSC> measurement.

References

[1] S.E. Rantz, Measurement and Computation of Streamflow, U.S. Geol. Surv. Water Supply Pap. 2175. 1 (1982). http://www.mendeley.com/catalog/measurement-computation-streamflow-volume-1-measurement-stage-discharge/ (accessed April 29, 2015).

[2] J. Jalbert, T. Mathevet, A.C. Favre, Temporal uncertainty estimation of discharges from rating curves using a variographic analysis, J. Hydrol. 397 (2011) 83–92. doi:10.1016/j.jhydrol.2010.11.031.

[3] A. Petersen-Øverleir, A. Soot, T. Reitan, Bayesian Rating Curve Inference as a Streamflow Data Quality Assessment Tool, Water Resour. Manag. 23 (2009) 1835–1842. doi:10.1007/s11269-008-9354-5.

[4] B.M. Fekete, C.J. Vörösmarty, The current status of global river discharge monitoring and potential new technologies complementing traditional discharge measurements, Predict. Ungauged Basins PUB Kick-off (Proceedings PUB Kick-off Meet. Held Bras. Novemb. 2002), IAHS Publ. No. 309. (2007) 129–136.

[5] D.M. Bjerklie, S. Lawrence Dingman, C.J. Vorosmarty, C.H. Bolster, R.G. Congalton, Evaluating the potential for measuring river discharge from space, J. Hydrol. 278 (2003) 17–38. doi:10.1016/S0022-1694(03)00129-X.

[6] D.M. Hannah, S. Demuth, H.A.J. van Lanen, U. Looser, C. Prudhomme, G. Rees, et al., Large-scale river flow archives: importance, current status and future needs, Hydrol. Process. 25 (2011) 1191–1200. doi:10.1002/hyp.7794.

[7] A.I.M. M.P. Mosley, Streamflow, D.R. Maidment (Ed.), Handbook of Hydrology., McGraw-Hill, New York, 1992.

[8] G.C.L. David, C.J. Legleiter, E. Wohl, S.E. Yochum, Characterizing spatial variability in velocity and turbulence intensity using 3-D acoustic Doppler velocimeter data in a plane-bed reach of East St. Louis Creek, Colorado, USA, Geomorphology. 183 (2013) 28–44. doi:10.1016/j.geomorph.2012.07.026.

[9] D. Kim, M. Muste, Multi-dimensional representation of river hydrodynamics using ADCP data processing software, Environ. Model. Softw. 38 (2012) 158–166. doi:10.1016/j.envsoft.2012.05.011.

[10] A.E. Hay, L. Zedel, R. Cheel, J. Dillon, On the vertical and temporal structure of flow and stress within the turbulent oscillatory boundary layer above evolving sand ripples, Cont. Shelf Res. 46 (2012) 31–49. doi:10.1016/j.csr.2012.02.009.

[11] K. Klepiszewski, S. Seiffert, E. Henry, R. Erpelding, S. Fonck, Feasibility Study on the

Monitoring of Internal Flow and Transport Processes in Combined Sewer Overflow and Waste Water Treatment Structures, in: 9th Int. Symp. Ultrason. Doppler Methods Fluid Mech. Fluid Eng., 2014: pp. 17–20.

[12] D. Hurther, P.D. Thorne, M. Bricault, U. Lemmin, J.-M. Barnoud, A multi-frequency Acoustic Concentration and Velocity Profiler (ACVP) for boundary layer measurements of fine-scale flow and sediment transport processes, Coast. Eng. 58 (2011) 594–605. doi:10.1016/j.coastaleng.2011.01.006.

[13] H. Zheng, Design velocity coastal of sea the acoustic with tomography an system for to the measurement application, 3 (1998) 199–210.

[14] J.L. Best, R.A. Kostaschuk, P. V. Villard, Quantitative visualization of flow fields associated with alluvial sand dunes: Results from the laboratory and field using ultrasonic and acoustic doppler anemometry, J. Vis. 4 (2001) 373–381. doi:10.1007/BF03183900.

[15] Y. Nihei, A. Kimizu, A new monitoring system for river discharge with horizontal acoustic Doppler current profiler measurements and river flow simulation, Water Resour. Res. 46 (2010) 1–15. doi:10.1029/2008WR006970.

[16] G. Nord, F. Gallart, N. Gratiot, M. Soler, I. Reid, D. Vachtman, et al., Applicability of acoustic Doppler devices for flow velocity measurements and discharge estimation in flows with sediment transport, J. Hydrol. 509 (2014) 504–518. doi:10.1016/j.jhydrol.2013.11.020.

[17] P.D. Thorne, D.M. Hanes, A review of acoustic measurement of small-scale sediment processes, Cont. Shelf Res. 22 (2002) 603–632. doi:10.1016/S0278-4343(01)00101-7.

[18] M. Guerrero, The investigation of sediment processes in rivers by means of the Acoustic Doppler Profiler, Proc. Int. Assoc. Hydrol. Sci. 364 (2014) 368–373. doi:10.5194/piahs-364-368-2014.

[19] J.E. Costa, K.R. Spicer, R.T. Cheng, F.P. Haeni, N.B. Melcher, E.M. Thurman, et al., measuring stream discharge by non-contact methods: A Proof-of-Concept Experiment, Geophys. Res. Lett. 27 (2000) 553–556. doi:10.1029/1999GL006087.

[20] D.S. Mueller, extrap: Software to assist the selection of extrapolation methods for moving-boat ADCP streamflow measurements, Comput. Geosci. 54 (2013) 211–218. doi:10.1016/j.cageo.2013.02.001.

[21] Teledyne RD Instruments, Streampro ADCP., TELEDYNE RD INSTRUMENTS. (2006). http://rdinstruments.com/product/adcp/streampro-adcp.

[22] K. Lee, H.-C. Ho, M. Marian, C.-H. Wu, Uncertainty in open channel discharge measurements acquired with StreamPro ADCP, J. Hydrol. 509 (2014) 101–114. doi:10.1016/j.jhydrol.2013.11.031.

[23] R. Marsden, Streampro ADCP performance characteristics, in: Proc. IEEE/OES Eighth Work. Conf. Curr. Meas. Technol. 2005., IEEE, n.d.: pp. 90–92. doi:10.1109/CCM.2005.1506346.

[24] C.M. García, L. Tarrab, K. Oberg, R. Szupiany, M.I. Cantero, Variance of Discharge Estimates Sampled Using Acoustic Doppler Current Profilers from Moving Platforms, J. Hydraul. Eng. 138 (2012) 684–694. doi:10.1061/(ASCE)HY.1943-7900.0000558.

[25] Z. Chen, Z. Wang, Y. Liu, S. Wang, C. Leng, Estimating the flow velocity and discharge of ADCP unmeasured area in tidal reach, Flow Meas. Instrum. (2016). doi:10.1016/j.flowmeasinst.2016.10.009.

[26] M.W. Yoo, Y. Do Kim, S. Lyu, I.W. Seo, Flowrate and Velocity Measurement in Nakdong River Using ADCP, in: Adv. Water Resour. Hydraul. Eng., Springer Berlin Heidelberg, Berlin, Heidelberg, 2009: pp. 1946–1950. doi:10.1007/978-3-540-89465-0_333.

[27] F. De Serio, M. Mossa, Analysis of mean velocity and turbulence measurements with ADCPs, Adv. Water Resour. 81 (2014) 172–185. doi:10.1016/j.advwatres.2014.11.006.

[28] J.N. Goundar, M.R. Ahmed, Marine current energy resource assessment and design of a marine current turbine for Fiji, Renew. Energy. 65 (2014) 14–22. doi:10.1016/j.renene.2013.06.036.

[29] J. Lee, J.T. Liu, C.-C. Hung, S. Lin, X. Du, River plume induced variability of suspended particle characteristics, Mar. Geol. 380 (2016) 219–230. doi:10.1016/j.margeo.2016.04.014.

[30] K.C. Riffe, S.M. Henderson, J.C. Mullarney, Wave dissipation by flexible vegetation, Geophys. Res. Lett. 38 (2011) 1–5. doi:10.1029/2011GL048773.

[31] I. Kim, J.L. Lee, J.S. Hwang, S. Lee, J. Lee, Vertical Structure of Rip Current Observed at Haeundae Beach, J. Coast. Res. 72 (2014) 1–5. doi:10.2112/SI72-001.1.

[32] M. Simpson, Discharge Measurements using a Broad-Band Acoustic Doppler Current Profiler, Open Rep. 1 (2001) 01.

[33] L. Tarrab, C.M. García, M.I. Cantero, K. Oberg, Role of turbulence fluctuations on uncertainties of acoustic Doppler current profiler discharge measurements, Water Resour. Res. 48 (2012) 1–12. doi:10.1029/2011WR011185.

[34] J. Downing, Twenty-five years with OBS sensors: The good, the bad, and the ugly, Cont. Shelf Res. 26 (2006) 2299–2318. doi:10.1016/j.csr.2006.07.018.

[35] T.F. Sutherland, P.M. Lane, C.L. Amos, J. Downing, The calibration of optical backscatter sensors for suspended sediment of varying darkness levels, Mar. Geol. 162

(2000) 587–597. doi:10.1016/S0025-3227(99)00080-8.

[36] J. Yu, J. Jiang, D. Gong, S. Li, Y. Xu, Determining suspended sediment concentration and settling velocity from PC-ADP measurements in the Beibu Gulf, China, Chinese J. Oceanol. Limnol. 29 (2011) 691–701. doi:10.1007/s00343-011-0164-x.

[37] H.K. Ha, W.Y. Hsu, J.P.Y. Maa, Y.Y. Shao, C.W. Holland, Using ADV backscatter strength for measuring suspended cohesive sediment concentration, Cont. Shelf Res. 29 (2009) 1310–1316. doi:10.1016/j.csr.2009.03.001.

[38] M. BahreiniMotlagh, K. Kawanisi, X. Zhu, Acoustic Investigations of Tidal Bores, J. Japan Soc. Civ. Eng. Ser. B1 (Hydraulic Eng. 71 (2015) 139–144.

[39] J. Le Coz, G. Pierrefeu, A. Paquier, Evaluation of river discharges monitored by a fixed side-looking Doppler profiler, Water Resour. Res. 46 (2008) 1–13. doi:10.1029/2008WR006967.

[40] M.G. Sassi, A.J.F. Hoitink, B. Vermeulen, Discharge estimation from H-ADCP measurements in a tidal river subject to sidewall effects and a mobile bed, Water Resour. Res. 47 (2011) W06504. doi:10.1029/2010WR009972.

[41] J.W. Gartner, Estimating suspended solids concentrations from backscatter intensity measured by acoustic Doppler current profiler in San Francisco Bay, California, Mar. Geol. 211 (2004) 169–187. doi:10.1016/j.margeo.2004.07.001.

[42] M. Guerrero, N. Rüther, R. Archetti, Comparison under controlled conditions between multi-frequency ADCPs and LISST-SL for investigating suspended sand in rivers, Flow Meas. Instrum. 37 (2014) 73–82. doi:10.1016/j.flowmeasinst.2014.03.007.

[43] V. Defendi, V. Kovačević, F. Arena, L. Zaggia, Estimating sediment transport from acoustic measurements in the Venice Lagoon inlets, Cont. Shelf Res. 30 (2010) 883–893. doi:10.1016/j.csr.2009.12.004.

[44] J.J. Nauw, L.M. Merckelbach, H. Ridderinkhof, H.M. van Aken, Long-term ferry-based observations of the suspended sediment fluxes through the Marsdiep inlet using acoustic Doppler current profilers, J. Sea Res. 87 (2014) 17–29. doi:10.1016/j.seares.2013.11.013.

[45] K. Kawanisi, M. Razaz, K. Ishikawa, J. Yano, M. Soltaniasl, Continuous measurements of flow rate in a shallow gravel-bed river by a new acoustic system, Water Resour. Res. 48 (2012) 1–10. doi:10.1029/2012WR012064.

[46] K. Yamaguchi, J. Lin, A. Kaneko, T. Yayamoto, N. Gohda, H.Q. Nguyen, et al., A continuous mapping of tidal current structures in the kanmon strait, J. Oceanogr. 61 (2005) 283–294. doi:10.1007/s10872-005-0038-y.

[47] C.-F. Huang, N. Taniguchi, Y.-H. Chen, J.-Y. Liu, Estimating temperature and current

using a pair of transceivers in a harbor environment, J. Acoust. Soc. Am. 140 (2016) EL137-EL142. doi:10.1121/1.4959069.

[48] K. Kawanisi, M. Razaz, A. Kaneko, S. Watanabe, Long-term measurement of stream flow and salinity in a tidal river by the use of the fluvial acoustic tomography system, J. Hydrol. 380 (2010) 74–81. doi:10.1016/j.jhydrol.2009.10.024.

[49] K. Kawanisi, M. BahrainiMotlagh, M. AlSawaf, M. Razaz, High-frequency streamflow acquisition and bed level/flow angle estimates in a mountainous river using shallow-water acoustic tomography, Hydrol. Process. (2016) n/a-n/a. doi:10.1002/hyp.10796.

[50] M. Razaz, K. Kawanisi, I. Nistor, S. Sharifi, An acoustic travel time method for continuous velocity monitoring in shallow tidal streams, Water Resour. Res. 49 (2013) 4885–4899. doi:10.1002/wrcr.20375.

[51] R.N. Baer, M.J. Jacobson, Analysis of the effect of a Rossby wave on sound speed in the ocean, J. Acoust. Soc. Am. 55 (1974) 1178. doi:10.1121/1.1914683.

[52] X. Zhao, D. Wang, Ocean acoustic tomography from different receiver geometries using the adjoint method, J. Acoust. Soc. Am. 138 (2015) 3733–3741. doi:10.1121/1.4938232.

[53] A.C. Kibblewhite, D.G. Browning, The identification of major oceanographic fronts by long range acoustic propagation measurements, Deep Sea Res. 25 (1978) 1107–1118. doi:10.1016/0146-6291(78)90588-X.

[54] E. Richards, G. Potty, Acoustic interface treatment with an adjoint operator for linear range-dependent ocean index of refraction inversions, J. Acoust. Soc. Am. 133 (2013) 3528. doi:10.1121/1.4806356.

[55] W. Munk, C. Wunsch, Ocean acoustic tomography: a scheme for large scale monitoring, Deep Sea Res. Part A. Oceanogr. Res. Pap. 26 (1979) 123–161. doi:10.1016/0198-0149(79)90073-6.

[56] F. Gaillard, Evaluating the information content of tomographic data: Application to mesoscale observations, J. Geophys. Res. 97 (1992) 15489. doi:10.1029/92JC01295.

[57] U. Send, P.F. Worcester, B.D. Cornuelle, C.O. Tiemann, B. Baschek, Integral measurements of mass transport and heat content in the Strait of Gibraltar from acoustic transmissions, Deep Sea Res. Part II Top. Stud. Oceanogr. 49 (2002) 4069–4095. doi:10.1016/S0967-0645(02)00143-1.

[58] D. Behringer, T. Birdsall, M. Brown, B. Cornuelle, R. Heinmiller, R. Knox, et al., A demonstration of ocean acoustic tomography, Nature. 299 (1982) 121–125. doi:10.1038/299121a0.

[59] K. Kawanisi, A. Kaneko, S. Nigo, M. Soltaniasl, New acoustic system for continuous

measurement of river discharge and water temperature, Water Sci. Eng. 3 (2010) 47–55. doi:10.3882/j.issn.1674-2370.2010.01.005.

[60] M. Soltaniasl, K. Kawanisi, J. Yano, K. Ishikawa, Variability in salt flux and water circulation in Ota River Estuary , Japan, 6 (2013) 283–295. doi:10.3882/j.issn.1674-2370.2013.03.005.

[61] M. Razaz, K. Kawanisi, A. Kaneko, I. Nistor, Application of acoustic tomography to reconstruct the horizontal flow velocity field in a shallow river, Water Resour. Res. 51 (2015) 9665–9678. doi:10.1002/2015WR017102.

[62] M. Bahreinimotlagh, K. Kawanisi, M.M. Danial, M.B. Al Sawaf, J. Kagami, Application of shallow-water acoustic tomography to measure flow direction and river discharge, Flow Meas. Instrum. 51 (2016) 30–39. doi:10.1016/j.flowmeasinst.2016.08.010.

[63] K. Kawanisi, X. Zhu, X. Fan, I. Nistor, Monitoring Tidal Bores using Acoustic Tomography System, J. Coast. Res. (2016). doi:10.2112/JCOASTRES-D-15-00172.1.

[64] JAE-HUN PARK and ARATA KANEKO, Computer Simulation of Coastal Acoustic Tomography by a Two-Dimensional Vortex Model, J. Oceanogr. 57 (2001) 593–602.

[65] C. Zhang, A. Kaneko, X.-H. Zhu, B.M. Howe, N. Gohda, Acoustic measurement of the net transport through the Seto Inland Sea, Acoust. Sci. Technol. 37 (2016) 10–20. doi:10.1250/ast.37.10.

[66] Y. Adityawarman, Advanced design of the coastal acoustic tomography system and its application to environmental monitoring of the Seto Inland Sea, 2011.

[67] M. and S.O. Okujima, Observation of underwater ultrasound propagation in the sea by two-period M-sequence signal method, Japanese J. Appl. Phys.,. 20 (1981) 237–239.

[68] M.K. Simon, J.K. Omura, R. a Scholtz, Spread Spectrum Communications Handbook, 1985.

[69] Y.T. and A.K. HONG ZHENG, NORIAKI GOHDA, HIDEAKI NOGUCHI, TOSHIMICHI ITO, HARUHIKO YAMAOKA, TADASHI TAMURA, Reciprocal Sound Transmission Experiment for Current Measurement in the Seto Inland Sea , Japan, J. Oceanogr. 53 (1997) 117–127.

[70] W. Munk, C. Wunsch, Ocean acoustic tomography: a scheme for large scale monitoring, Deep Sea Res. Part A. Oceanogr. Res. Pap. 26 (1979) 123–161. doi:10.1016/0198-0149(79)90073-6.

[71] K. Kawanisi, S. Watanabe, A. Kaneko, T. Abe, River Acoustic Tomography for Continuous Measurement of Water Discharge, in: 3rd Int. Conf. Exhib. “Underwater Acoust. Meas. Technol. Results,” 2009: pp. 613–620.

[72] R.J. Urick, The Absorption of Sound in Suspensions of Irregular Particles, J. Acoust. Soc. Am. 20 (1948) 283. doi:10.1121/1.1906373.

[73] S.D. Richards, A.D. Heathershaw, P.D. Thorne, The effect of suspended particulate matter on sound attenuation in seawater, J. Acoust. Soc. Am. 100 (1996) 1447. doi:10.1121/1.415991.

[74] R.E. Francois, Sound absorption based on ocean measurements. Part II: Boric acid contribution and equation for total absorption, J. Acoust. Soc. Am. 72 (1982) 1879. doi:10.1121/1.388673.

[75] J. Sheng, An examination of the spherical scatterer approximation in aqueous suspensions of sand, J. Acoust. Soc. Am. 83 (1988) 598. doi:10.1121/1.396153.

[76] J.H. Simpson, N.R. Fisher, P. Wiles, Reynolds stress and TKE production in an estuary with a tidal bore, Estuar. Coast. Shelf Sci. 60 (2004) 619–627. doi:10.1016/j.ecss.2004.03.006.

[77] B. VERMEULEN, A. HOITINK, M. SASSI, On the use of horizontal acoustic Doppler profilers for continuous bed shear stress monitoring, Int. J. Sediment Res. 28 (2013) 260–268. doi:10.1016/S1001-6279(13)60037-2.

[78] F.G. Latosinski, R.N. Szupiany, C.M. García, M. Guerrero, M.L. Amsler, Estimation of Concentration and Load of Suspended Bed Sediment in a Large River by Means of Acoustic Doppler Technology, J. Hydraul. Eng. (2014) 1–15. doi:10.1061/(ASCE)HY.1943-7900.0000859.

[79] A. Downing, P.D. Thorne, C.E. Vincent, Backscattering from a suspension in the near field of a piston transducer, J. Acoust. Soc. Am. 97 (1995) 1614. doi:10.1121/1.412100.

[80] T.H. Lee, D.M. Hanes, Direct inversion method to measure the concentration profile of suspended particles using backscattered sound, J. Geophys. Res. 100 (1995) 2649. doi:10.1029/94JC03068.

[81] P.D. Thorne, D. Hurther, An overview on the use of backscattered sound for measuring suspended particle size and concentration profiles in non-cohesive inorganic sediment transport studies, Cont. Shelf Res. 73 (2014) 97–118. doi:10.1016/j.csr.2013.10.017.

[82] a. J.F. Hoitink, P. Hoekstra, Observations of suspended sediment from ADCP and OBS measurements in a mud-dominated environment, Coast. Eng. 52 (2005) 103–118. doi:10.1016/j.coastaleng.2004.09.005.

[83] S.M. Siadatmousavi, F. Jose, Q. Chen, H.H. Roberts, Comparison between optical and acoustical estimation of suspended sediment concentration: Field study from a muddy coast, Ocean Eng. 72 (2013) 11–24. doi:10.1016/j.oceaneng.2013.06.002.

[84] F.B. Jensen, W.A. Kuperman, M.B. Porter, H. Schmidt, Computational Ocean Acoustics, Springer New York, New York, NY, 2011. doi:10.1007/978-1-4419-8678-8.

[85] H.Q. Nguyen, A. Kaneko, J. Lin, K. Yamaguchi, N. Gohda, Y. Takasugi, Acoustic measurement of multisubtidal internal modes generated in Hiroshima Bay, Japan, IEEE J. Ocean. Eng. 34 (2009) 103–112. doi:10.1109/JOE.2009.2014933.

[86] J.L. Reis, a S. Martinho, a a Pires-Silva, a J. Silva, Assessing the Influence of the River Discharge on the Minho Estuary Tidal Regime, J. Coast. Res. 2009 (2009) 1405–1409.

[87] Q. Mao, P. Shi, K. Yin, J. Gan, Y. Qi, Tides and tidal currents in the Pearl River Estuary, Cont. Shelf Res. 24 (2004) 1797–1808. doi:10.1016/j.csr.2004.06.008.

[88] Z. Chen, S. Wang, Z. Wang, A new interpolation scheme for detiding vessel-mounted ADCP data in tidal reach of Yangtze Estuary, Flow Meas. Instrum. 50 (2016) 185–196. doi:10.1016/j.flowmeasinst.2016.06.018.

[89] C. Flener, Y. Wang, L. Laamanen, E. Kasvi, J.-M. Vesakoski, P. Alho, Empirical Modeling of Spatial 3D Flow Characteristics Using a Remote-Controlled ADCP System: Monitoring a Spring Flood, Water. 7 (2015) 217–247. doi:10.3390/w7010217.

[90] J.H. Simpson, E.G. Mitchelson-Jacob, A.E. Hill, Flow structure in a channel from an acoustic Doppler current profiler, Cont. Shelf Res. 10 (1990) 589–603. doi:10.1016/0278-4343(90)90083-X.

[91] A. Isobe, T. Kuramitsu, H. Nozaki, P.-H. Chang, Reliability of ADCP data detided with a numerical model on the East China Sea shelf, J. Oceanogr. 63 (2007) 135–141. doi:10.1007/s10872-007-0011-z.

[92] L. Chintu, Numerical modeling of unsteady open-channel flow, Adv. Hydrosci. 14 (1986) 161–254.

[93] H.C. Lien, J.C.Y. T. Y. Hsieh, BEND-FLOW SIMULATION USING 2D DEPTH-AVERAGED MODEL, J. Hydraul. Eng. 125 (1999) 1097–1108.

[94] D.V.H. Struiksma N, Olesen KW, Flokstra C, Bed deforma- tion in curved alluvial channels, J Hydraul Res. 23 (1985) 1985.

[95] N. Struiksma, Analysis of a 2-D bed topography model for rivers, river meandering., Am Geophys Union. (1989) 153 – 80.

[96] D.W. Crowder, P. Diplas, Using two-dimensional hydrodynamic models at scales of ecological importance, J. Hydrol. 230 (2000) 172–191. doi:10.1016/S0022-1694(00)00177-3.

[97] and O.G.T. Norton W. R., King I. P., A finite element model for lower granite reservoir., Rep. Prep. Walla Dist. U.S. Army Corps Eng. Water Resour. Eng. Inc., Walnut Creek,

Calif. (1973).

[98] I.P. King, Program Documentation: RMA2-A Two-Dimensional Finite Element Model for Flow in Estuaries and Streams., Ver 4.3. Resour. Manag. Assoc. Lafayette, CA. (1990).

[99] G. Chung, K.E. Lansey, T.W. Kim, J.H. Kim, Two-Dimensional Flood Modeling of the Santa Cruz River in Tucson, Arizona Using RMA2, in: Crit. Transitions Water Environ. Resour. Manag., American Society of Civil Engineers, Reston, VA, 2004: pp. 1–11. doi:10.1061/40737(2004)299.

[100] M. Gałek, P.S. Hachaj, Application of the RMA2/RMA4 Models to Simulate Pollution Transport in a Retention Reservoir, in: Springer Berlin Heidelberg, 2013: pp. 301–313. doi:10.1007/978-3-642-30209-1_21.

[101] W.A. Donnell B.P., Letter, J.V., Jr., McAnally, W.H., and Thomas, Users guide to RMA2 WES Version 4.5, U.S. Army Corps Eng. Waterw. Exp. Stn. (2000) 264.

[102] U.S.A.C. of E. (USACE)., User's guide to RAM2 Version 4.3 , Waterways Experiment Station - Hydraulics Laboratory., Prod. by WesTech Syst. Inc., New York. (1996) 1996.

Appendix 1. Formulation of relative error of angle estimation

$$\frac{\delta\theta}{\theta} = \frac{\delta\theta_{\emptyset}}{\theta} + \frac{\delta\theta_{A_1}}{\theta} + \frac{\delta\theta_{A_2}}{\theta} + \frac{\delta\theta_{u_1}}{\theta} + \frac{\delta\theta_{u_2}}{\theta}$$

where

$$\frac{\delta\theta_{\emptyset}}{\theta} = \frac{(0.25(-1.41\sqrt{A_1{}^2u_1{}^2 + 6.A_1A_2u_1u_2 + A_2{}^2u_2{}^2 + (A_1u_1 - 1.A_2u_2)^2\text{Cos}[2.\phi]}\text{Sin}[\phi] - 2.(-1.A_1u_1 + A_2u_2)\text{Sin}[2.\phi] - \frac{1.41(A_1u_1 - 1.A_2u_2)^2\text{Cos}[\phi]\text{Sin}[2.\phi]}{\sqrt{A_1{}^2u_1{}^2 + 6.A_1A_2u_1u_2 + A_2{}^2u_2{}^2 + (A_1u_1 - 1.A_2u_2)^2\text{Cos}[2.\phi]}}))}{(A_1u_1 + A_2u_2)\theta}$$

,

$$\frac{\delta\theta_{A_1}}{\theta} = \frac{0.25(\frac{3.u_1 - 1.u_1\text{Cos}[2.\phi] + \frac{0.70\,\text{Cos}[\phi](2.A_1u_1{}^2 + 6.A_2u_1u_2 + 2.\text{u1}(A_1u_1 - 1.A_2u_2)\text{Cos}[2.\phi])}{\sqrt{A_1{}^2u_1{}^2 + 6.A_1A_2u_1u_2 + A_2{}^2u_2{}^2 + (A_1u_1 - 1.A_2u_2)^2\text{Cos}[2.\phi]}}}{A_1u_1 + A_2u_2} - \frac{1.u_1(3.A_1u_1 + A_2u_2 + (-1.A_1u_1 + A_2u_2)\text{Cos}[2.\phi] + 1.41\text{Cos}[\phi]\sqrt{A_1{}^2u_1{}^2 + 6.A_1A_2u_1u_2 + A_2{}^2u_2{}^2 + (A_1u_1 - 1.A_2u_2)^2\text{Cos}[2.\phi]})}{(A_1u_1 + A_2u_2)^2}))}{\theta}$$

,

$$\frac{\delta\theta_{A2}}{\theta}$$

$$= \frac{(0.25(\frac{u_2 + u_2\text{Cos}[2.\phi] + \frac{0.70\text{Cos}[\phi](6.A_1u_1u_2 + 2.A_2{u_2}^2 - 2.u_2(A_1u_1 - 1.A_2u_2)\text{Cos}[2.\phi])}{\sqrt{{A_1}^2{u_1}^2 + 6.A_1A_2u_1u_2 + {A_2}^2{u_2}^2 + (A_1u_1 - 1.A_2u_2)^2\text{Cos}[2.\phi]}}}{A_1u_1 + A_2u_2} - \frac{1.u_2(3.A_1u_1 + A_2u_2 + (-1.A_1u_1 + A_2u_2)\text{Cos}[2.\phi] + 1.41\text{Cos}[\phi]\sqrt{{A_1}^2{u_1}^2 + 6.A_1A_2u_1u_2 + {A_2}^2{u_2}^2 + (A_1u_1 - 1.A_2u_2)^2\text{Cos}[2.\phi]})}{(A_1u_1 + A_2u_2)^2}))}{\theta}$$

,

$$\frac{\delta\theta_{u_1}}{\theta}$$

$$= \frac{(0.25(\frac{3.A_1 - 1.A_1\text{Cos}[2.\phi] + \frac{0.70\text{Cos}[\phi](2.{A_1}^2u_1 + 6.A_1A_2u_2 + 2.A_1(A_1u_1 - 1.A_2u_2)\text{Cos}[2.\phi])}{\sqrt{{A_1}^2{u_1}^2 + 6.A_1A_2u_1u_2 + {A_2}^2\text{u}2^2 + (A_1u_1 - 1.A_2u_2)^2\text{Cos}[2.\phi]}}}{A_1u_1 + A_2u_2} - \frac{1.A_1(3.A_1u_1 + A_2u_2 + (-1.A_1u_1 + A_2u_2)\text{Cos}[2.\phi] + 1.41\text{Cos}[\phi]\sqrt{{A_1}^2{u_1}^2 + 6.A_1A_2u_1u_2 + {A_2}^2{u_2}^2 + (A_1u_1 - 1.A_2u_2)^2\text{Cos}[2.\phi]})}{(A_1u_1 + A_2u_2)^2}))}{\theta}$$

,

$$\frac{\delta\theta_{u_2}}{\theta}$$

$$= \frac{(0.25(\frac{A_2 + A_2\text{Cos}[2.\phi] + \frac{0.70\text{Cos}[\phi](6.A_1A_2u_1 + 2.{A_2}^2u_2 - 2.A_2(A_1u_1 - 1.A_2u_2)\text{Cos}[2.\phi])}{\sqrt{{A_1}^2{u_1}^2 + 6.A_1A_2u_1u_2 + {A_2}^2{u_2}^2 + (A_1u_1 - 1.A_2u_2)^2\text{Cos}[2.\phi]}}}{A_1u_1 + A_2u_2} - \frac{1.A_2(3.A_1u_1 + A_2u_2 + (-1.A_1u_1 + A_2u_2)\text{Cos}[2.\phi] + 1.41\text{Cos}[\phi]\sqrt{{A_1}^2{u_1}^2 + 6.A_1A_2u_1u_2 + {A_2}^2{u_2}^2 + (A_1u_1 - 1.A_2u_2)^2\text{Cos}[2.\phi]})}{(A_1u_1 + A_2u_2)^2}))}{\theta}$$